

**UNCLASSIFIED**



**Australian Government**  
**Department of Defence**  
Defence Science and  
Technology Organisation

# Smoke Flow Visualisation and Particle Image Velocimetry Measurements over a Generic Submarine Model

*Peter Manovski, Matteo Giacobello and Paul Jacquemin*

**Aerospace Division**  
**Defence Science and Technology Organisation**

DSTO-TR-2944

## **ABSTRACT**

Experimental testing of a generic submarine model has been conducted in the DSTO low speed wind tunnel. These tests aimed to investigate the off-body flow-field around a generic submarine shape in its bare-hull configuration by performing smoke flow visualisation and gathering quantitative velocity data using particle image velocimetry (PIV). The PIV measurements were compared with computational fluid dynamic (CFD) results and good agreement was obtained. The tests also provided the opportunity to refine the application of the PIV technique in a large-scale wind tunnel facility. These experimental data will complement computational and experimental hydrodynamic analysis of the generic submarine shape.

## **RELEASE LIMITATION**

*Approved for public release*

**UNCLASSIFIED**

UNCLASSIFIED

*Published by*

*Aerospace Division  
DSTO Defence Science and Technology Organisation  
506 Lorimer St  
Fishermans Bend, Victoria 3207 Australia*

*Telephone: 1300 333 362  
Fax: (03) 9626 7999*

*© Commonwealth of Australia 2014  
AR-015-875  
March 2014*

**APPROVED FOR PUBLIC RELEASE**

UNCLASSIFIED

UNCLASSIFIED

# Smoke Flow Visualisation and Particle Image Velocimetry Measurements over a Generic Submarine Model

## Executive Summary

The Defence Science and Technology Organisation (DSTO) Undersea Warfare Corporate Enabling Research Program (CERP) is aimed at improving the general knowledge and understanding of the behaviour of complex flows around modern submarine shapes. The research involves the use of high-fidelity computational fluid dynamic (CFD) models, as well as experimental hydrodynamic and aerodynamic test techniques to investigate a common generic shape. The extensive dataset gathered from the variety of sources will enhance DSTO knowledge and understanding of these complex flows and in turn serves as validation data for computational methods.

This report documents the wind tunnel testing of the generic submarine model in the DSTO low speed wind tunnel (LSWT) in early 2011. The aim of the study was to characterise the flow-field around a generic submarine shape in its bare-hull configuration, that is, without the hull-casing, fin and control surfaces attached. Experiments were conducted on a 1.35 m long aluminium model with a diameter of 0.185 m. Smoke flow visualisation was used to provide qualitative information for the flow-field as the model was pitched and yawed. Particle Image Velocimetry (PIV) then provided two-dimensional quantitative velocity measurements along the centre-line of the model at various incidences.

Smoke visualisation results revealed that the flow-field at incidence was characterised by the formation of cross-flow separation near the tail, which migrated forward with increasing incidence. The PIV technique provided instantaneous and mean flow-fields, from which maps of the vorticity and Reynolds stress could be derived. With increasing incidence the PIV derived streamlines along the upper surface of the model displayed a local downwash which was consistent with the smoke visualisation results. The PIV results were compared with CFD results. The streamwise velocity and vorticity showed good agreement with the CFD results. PIV proved to be a useful and reliable technique for characterising the off-body flow-field around the generic submarine shape.

Further experimental testing of the model in the DSTO LSWT is planned, including additional PIV measurements with the hull-casing, fin and the control surfaces attached. The implementation of a range of improvements suggested in this report will provide DSTO researchers with an enhanced PIV capability for future test campaigns.

UNCLASSIFIED

UNCLASSIFIED

*This page is intentionally blank*

UNCLASSIFIED

## Authors



**P. Manovski**  
Aerospace Division

*Peter Manovski graduated from Monash University in 2005 completing a double degree in Bachelor of Engineering (Mechanical) and Bachelor of Technology (Aerospace) with First Class Honours. The following year he obtained employment with DSTO at Melbourne. Working in Flight Systems Branch, he has gained experience in experimental aerodynamics and using advanced flow diagnostics techniques, such as Schlieren and particle image velocimetry (PIV). He had a pivotal role in commissioning DSTO's first PIV system and subsequently has conducted research into flow over cavities and submarine models. In 2008, he provided expert advice on store separation testing from the F-35 at the Arnold Engineering Development Centre, Tennessee. He was Lead Test Engineer for several test campaigns, including JASSM grid testing in the Transonic Wind Tunnel and Remus-100 force, moment and pressure tests in the Low Speed Wind Tunnel.*

---



**M. Giacobello**  
Aerospace Division

*Dr Matteo Giacobello completed an Aerospace Engineering degree in 1998 from the Royal Melbourne Institute of Technology. He joined DSTO in 1999 and has worked on a wide range of aerodynamic research problems. In 2005 Matteo received a Doctorate of Philosophy in Mechanical Engineering from the University of Melbourne. His current research interests include the optically based flow diagnostics techniques of Particle Image Velocimetry and Schlieren, and exploring the aerodynamics mechanisms of insect flight using numerical simulation. He is the current Science Team Lead, Aircraft & Weapons System Computational Fluid Dynamics in Flight Systems Branch.*

---



**P. Jacquemin**  
Aerospace Division

*Paul Jacquemin is a Senior Officer (Technical) in the Aerospace Division at DSTO. He received an Associate Diploma of Engineering (National) in Mechanical Engineering from the Western Melbourne Institute of TAFE. Prior to working at DSTO he designed the Mechanical and Electrical PLC systems for pneumatic conveying systems. He currently works in the Flight Systems Branch and conducts aerodynamic tests and provides technical support within the wind tunnel facilities. He recently upgraded the Low Speed Wind Tunnel electrical control and model support systems.*

---

# Contents

## NOTATION

<b>1. INTRODUCTION.....</b>	<b>1</b>
<b>2. EXPERIMENTAL TEST FACILITY AND MODEL.....</b>	<b>1</b>
<b>2.1 DSTO Low Speed Wind Tunnel.....</b>	<b>1</b>
<b>2.2 Generic Submarine Model.....</b>	<b>2</b>
2.2.1 Model Configuration .....	2
2.2.2 Support System.....	2
2.2.3 Blockage Ratio.....	2
2.2.4 Boundary Layer Transition .....	3
<b>3. EXPERIMENTAL METHOD .....</b>	<b>3</b>
<b>3.1 Smoke Flow Visualisation .....</b>	<b>3</b>
<b>3.2 Particle Image Velocimetry .....</b>	<b>4</b>
3.2.1 Axes System .....	6
<b>3.3 Derived Quantities .....</b>	<b>6</b>
3.3.1 Velocity .....	7
3.3.2 Mean Velocity .....	7
3.3.3 Vorticity and Velocity Gradients.....	8
3.3.4 Mean Vorticity .....	8
3.3.5 Turbulent Quantities.....	8
<b>3.4 Data Processing and Validation Criteria.....</b>	<b>9</b>
<b>3.5 Test Conditions .....</b>	<b>10</b>
<b>3.6 Particle Image Velocimetry Measurement Locations .....</b>	<b>11</b>
<b>4. RESULTS .....</b>	<b>14</b>
<b>4.1 Smoke Flow Visualisation .....</b>	<b>14</b>
<b>4.2 PIV Mean Flow-field.....</b>	<b>17</b>
4.2.1 Flow-field at Low Angles-of-Attack .....	17
4.2.2 Flow-field at High Angles-of-Attack .....	18
4.2.3 Reynolds Number Sensitivity Study .....	25
<b>4.3 Comparison of Experimental and Computational Results .....</b>	<b>26</b>
<b>4.4 Assessment of Data Quality.....</b>	<b>31</b>
4.4.1 Measurement Uncertainties .....	31
4.4.2 Convergence of Mean Flow Parameters .....	31
4.4.3 Assessment of Peak-Locking .....	32
<b>4.5 Lessons Learnt and Key Recommendations .....</b>	<b>33</b>
4.5.1 Surface Reflections .....	33
4.5.2 Optical Quality of Test Section Window.....	34
4.5.3 Seeding Losses .....	34
<b>5. CONCLUSIONS.....</b>	<b>36</b>

**6. ACKNOWLEDGEMENTS ..... 36**

**7. REFERENCES ..... 37**

**APPENDIX A: WIND SPEED MEASUREMENT ..... 39**  
**A.1. Wind Speed Measurement Uncertainty ..... 39**

**APPENDIX B: PIV MEASUREMENT SETTINGS ..... 41**

**APPENDIX C: PIV UNCERTAINTY ANALYSIS ..... 43**  
**C.1. PIV Measurement Uncertainty ..... 43**  
**C.2. Mean Velocity Uncertainty ..... 44**  
**C.3. Vorticity Uncertainty ..... 45**  
**C.4. Reynolds Stress Uncertainty ..... 48**

## List of Figures

Figure 1 - Generic submarine model mounted in the LSWT.....	3
Figure 2 - PIV measurement principle (image from Dantec Dynamics [5]) .....	5
Figure 3 - PIV arrangement with the model mounted in LSWT.....	6
Figure 4 - The location and size of the three PIV field-of-views with respect to the model tail. (All dimensions are in mm.).....	13
Figure 5 - The amalgamation of the three PIV field-of-views with respect to the model body. (All dimensions are in mm.) .....	13
Figure 6 - Smoke flow visualisation patterns on the starboard side of the submarine model with increasing angle-of-attack (a) $\alpha = 0^\circ$ , (b) $\alpha = 2.5^\circ$ , (c) $\alpha = 5^\circ$ and (d) $\alpha = 15^\circ$ . <sup>1</sup> .....	15
Figure 7 - Cross-flow separation on a prolate spheroid at pitch (from Chesnakas and Simpson [16]) .....	16
Figure 8 - Smoke flow visualisation at $\alpha = 15^\circ$ and $\beta = 0^\circ$ , showing attached flow along the centre-line of the model.....	16
Figure 9 - Smoke flow visualisation at $\alpha = 0^\circ$ and $\beta = 30^\circ$ , showing roll-up of the vortex sheets into two distinct vortices .....	16
Figure 10 - Smoke flow visualisation at $\alpha = 0^\circ$ and $\beta = 0^\circ$ , with probe positioned at the aft fairing cut-out showing a recirculation region and an unsteady wake.....	17
Figure 11 - Smoke flow visualisation at $\alpha = 0^\circ$ and $\beta = 30^\circ$ , showing vortex shedding from the pitch actuator arm.....	17
Figure 12 - (a) Streamline topology overlayed with non-dimensional streamwise velocity, (b) non-dimensional out-of-plane vorticity, (c) Reynolds stress contours at $\alpha = 0^\circ$ .....	19
Figure 13 - (a) Streamline topology overlayed with non-dimensional streamwise velocity, (b) non-dimensional out-of-plane vorticity, (c) Reynolds stress contours at $\alpha = -2.5^\circ$ .....	20
Figure 14 - (a) Streamline topology overlayed with non-dimensional streamwise velocity, (b) non-dimensional out-of-plane vorticity, (c) Reynolds stress contours at $\alpha = 2.5^\circ$ .....	21
Figure 15 - (a) Streamline topology overlayed with non-dimensional streamwise velocity, (b) non-dimensional out-of-plane vorticity, (c) Reynolds stress contours at $\alpha = 5^\circ$ .....	22
Figure 16 - (a) Streamline topology overlayed with non-dimensional streamwise velocity, (b) non-dimensional out-of-plane vorticity, (c) Reynolds stress contours at $\alpha = 10^\circ$ .....	23
Figure 17 - (a) Streamline topology overlayed with non-dimensional streamwise velocity, (b) non-dimensional out-of-plane vorticity, (c) Reynolds stress contours at $\alpha = 15^\circ$ .....	24
Figure 18 - Ensemble-averaged, (a) non-dimensional streamwise velocity ( $\bar{u}/U_\infty$ ), (b) non-dimensional out-of-plane vorticity ( $\bar{\omega}_z L/U_\infty$ ), (c) Reynolds stress ( $-\overline{u'v'}/U_\infty^2$ ) contours for field-of-view 1, $\alpha = 0^\circ$ and for freestream velocities of 20, 30 and 40 m/s.....	26
Figure 19 - The CFD surface model of the generic submarine including the support fairing and actuator arm [19].....	27
Figure 20 - Comparison between CFD generated non-dimensional streamwise velocity ( $\bar{u}/U_\infty$ ) and PIV results, at $\alpha = 10^\circ$ .....	28
Figure 21 - Comparison between CFD generated non-dimensional out-of-plane vorticity ( $\bar{\omega}_z L/U_\infty$ ) and PIV results, at $\alpha = 10^\circ$ .....	28
Figure 22 - Comparison between CFD generated Reynolds stress ( $-\overline{u'v'}/U_\infty^2$ ) contours and PIV results, at $\alpha = 10^\circ$ .....	28

Figure 23 - CFD and PIV non-dimensional streamwise velocity profiles at $\alpha = 0^\circ$ , at locations, (a) $x/L = -0.059$ , (b) $x/L = -0.02$ , (c) $x/L = 0.011$ and (d) $x/L = 0.05$ .....	29
Figure 24 - CFD and PIV non-dimensional out-of-plane vorticity profiles at $\alpha = 0^\circ$ , at locations (a) $x/L = -0.059$ , (b) $x/L = -0.02$ , (c) $x/L = 0.011$ and (d) $x/L = 0.05$ .....	30
Figure 25 - Running average plots of (a) streamwise velocity ( $\bar{u}$ ), (b) vertical velocity ( $\bar{v}$ ) and (c) normalised u-component velocity fluctuation ( $\bar{u}'/U_\infty$ ), v-component velocity fluctuation ( $\bar{v}'/U_\infty$ ) and Reynolds stress ( $\overline{u'v'}/U_\infty^2$ ) at $\alpha = 15^\circ$ for field-of-view 3 at $\{x/L, y/L\} = \{-0.0280, 0.0025\}$ . .....	32
Figure 26 - Histogram of PIV displacement data at $\alpha = -2.5^\circ$ and field-of-view 3, indicating unbiased pixel displacement. Histogram bin-width = 0.05 pixel.....	33
Figure 27 - Plot of spurious vector count over the number of fields taken at (a) $\alpha = 0^\circ$ and (b) $\alpha = 5^\circ$ , for field-of-view 1 at a freestream airspeed of 30 m/s. ....	35

## List of Tables

Table 1 - PIV test matrix.....	10
Table 2 - PIV test conditions and flow measurement parameters .....	11
Table 3 - Uncertainty of the normalised instantaneous and ensemble-averaged velocity, out-of-plane vorticity and Reynolds stress .....	31

## Notation

$D$	Model diameter (0.185 m)
$L$	Model reference length (1.35 m)
$L_c$	Characteristic length scale
$L_{scale}$	Calibration length (pixels)
$E_{disp}$	Uncertainty in the displacement measured by PIV
$E_{Pd}$	Differential pressure uncertainty
$E_{Ps}$	Static pressure uncertainty
$E_k$	Wind speed calibration factor uncertainty
$E_L$	Uncertainty in the model length
$E_{scale}$	Scaling uncertainty
$E_{time}$	Timing uncertainty
$E_T$	Uncertainty in the temperature of the test section
$E_{Total \bar{u}}$	Total fractional uncertainty in $\bar{U}$
$E_u$	PIV velocity uncertainty
$E_u^-$	Fractional uncertainty in PIV derived $\bar{u}$
$E \frac{\bar{u}}{U_\infty}$	Fractional uncertainty in normalised $\bar{u}$
$E_{u'^2}$	Fractional uncertainty in u turbulence intensity
$E_{u'v'}$	Fractional uncertainty in the PIV derived Reynolds stress
$E \frac{\overline{u'v'}}{U_\infty^2}$	Fractional uncertainty in the normalised Reynolds stress
$E_{U_\infty}$	Uncertainty in the freestream airspeed
$E_\rho$	Uncertainty in the density
$E_v^-$	Fractional uncertainty in $\bar{v}$
$E_{v'^2}$	Fractional uncertainty in v turbulence intensity
$E_{\sigma u}$	Fractional uncertainty in standard deviation of u
$E_{\sigma v}$	Fractional uncertainty in standard deviation of v
$E_\omega$	Fractional uncertainty in out-of-plane vorticity
$E_\omega^-$	Fractional uncertainty in mean out-of-plane vorticity
$E_{\frac{\omega_z L}{U_\infty}}$	Fractional uncertainty in mean normalised out-of-plane vorticity
$E_{obias}$	Bias uncertainty in out-of-plane vorticity
$E_{\omega pres}$	Precision uncertainty in out-of-plane vorticity
$E_{\omega pres}^-$	Precision uncertainty in mean out-of-plane vorticity
f	Generic function
i	Spatial coordinate index in the x direction

## UNCLASSIFIED

DSTO-TR-2944

$j$	Spatial coordinate index in the y direction
$M$	Image magnification
$N$	Number of PIV samples (image pairs or fields)
$P_d$	Differential pressure across the two piezoelectric rings (Pa)
$P_s$	Static pressure of the test section (Pa)
$R$	Ideal gas constant for air = 287.058 (J/KgK)
$R_o$	Local radius of model (m)
$R_{max}$	Maximum radius of model = $D/2$ (m)
$Re_L$	Reynolds number ( $\rho U_\infty L / \mu$ )
$t$	time (s)
$T$	Test section temperature (K)
$u$	Velocity component in the x (streamwise) direction (m/s)
$U_\infty$	Freestream velocity (m/s)
$\bar{u}$	Time-averaged u-component velocity (m/s)
$u'$	u-component turbulence intensity
$\overline{u'}$	Time-averaged u-component velocity fluctuation (m/s)
$v$	Velocity component in the y (vertical) direction (m/s)
$\bar{v}$	Time-averaged v-component velocity (m/s)
$v'$	v-component turbulence intensity
$\overline{v'}$	Time-averaged v-component velocity fluctuation (m/s)
$x$	Axial or streamwise distance (m) – parallel to freestream flow
$y$	Spanwise distance (m)
$w$	Velocity component in the z (cross-stream) direction (m/s)
$w'$	w-component turbulence intensity
$z$	Cross-stream distance (m)
$\alpha$	Angle-of-attack or pitch ( $^\circ$ )
$\beta$	Angle-of-sideslip or yaw ( $^\circ$ )
$\delta_{\Delta x}$	PIV algorithm minimum resolvable displacement (pixels)
$\delta_{scale}$	Scaling uncertainty (pixels)
$\delta_{time}$	Timing uncertainty (s)
$\delta_{Total\ scale}$	Total scaling uncertainty (pixels)
$\delta_{\omega z}$	Vorticity thickness
$\Delta$	Spatial separation of PIV measurements (m)
$\Delta t$	Time delay between laser pulses (s)
$\Delta X$	Particle displacement (pixels)
$\lambda$	Non-dimensional precision uncertainty transmission ratio
$\rho$	Density of air in the test section ( $kg/m^3$ )
$\mu$	Viscosity of air in the test section ( $kg/s\ m$ )
$\sigma_U$	Standard deviation (or $u_{RMS}$ ) in the u-component velocity
$\sigma_V$	Standard deviation (or $v_{RMS}$ ) in the v-component velocity
$\omega_{bias}$	Actual peak out-of-plane vorticity (1/s)
$\omega_{max}$	Peak PIV calculated out-of-plane vorticity (1/s)
$\omega_z$	Instantaneous out-of-plane vorticity (1/s)
$\overline{\omega_z}$	Time-averaged out-of-plane vorticity (1/s)

UNCLASSIFIED

# 1. Introduction

Researchers at the Defence Science and Technology Organisation (DSTO) have used smoke flow visualisation and particle image velocimetry (PIV) to assess the off-body flow characteristics around a model of a generic submarine. This work was conducted in the DSTO low speed wind tunnel (LSWT), with the secondary aim of refining the application of PIV methods when applied in a large-scale wind tunnel facility.

Smoke flow visualisation was used to provide a qualitative picture of the flow around the submarine model, and provided insight into the nature of the flow-field. The PIV measurements were then targeted at areas of interest, which included the tail and wake region of the model. This aft region is typically where the propeller is located, and at full-scale certain inflow conditions can lead to flow induced vibrations and noise.

This work was conducted under the DSTO Undersea Warfare - Corporate Enabling Research Program (CERP), and is part of a large research activity to improve general knowledge and understanding of the behaviour of complex flows around modern submarine shapes. This experiment is an extension of the force and moment tests of the generic submarine model conducted in the DSTO LSWT [1]. In addition to these experimental tests, the same model will also be tested in a hydrodynamic facility, with the results compared against those derived using computational fluid dynamics (CFD) methods.

This report documents the smoke flow visualisation and PIV testing in the LSWT including descriptions of the experimental equipment used, the wind tunnel model, and the test facility. The test methodology and the test conditions are also presented, together with selected results. The PIV results are compared qualitatively with the smoke visualisation and quantitatively, with CFD results. A number of key recommendations for future testing are also reported.

## 2. Experimental Test Facility and Model

### 2.1 DSTO Low Speed Wind Tunnel

Experiments were conducted in the DSTO LSWT facility located at Fishermans Bend in Melbourne. The facility is a conventional, continuous flow, closed-circuit, single-return wind tunnel with a contraction ratio of 4:1. The test section has an irregular octagonal shape and measures 2.74 m (wide)  $\times$  2.13 m (high)  $\times$  6.56 m (long). The tunnel is powered by a 660 kW electric motor driving a 3.96 m diameter 8-bladed fan. The facility is capable of a maximum airspeed of approximately 100 m/s when the test section is empty. Honeycomb consisting of triangle cells with dimensions 48 mm by 41 mm, and 127 mm long, is installed in the settling chamber. The freestream u-component turbulence intensity ( $u'$ ) is less than 0.4%, and the v and w component intensities ( $v'$ ,  $w'$ ) are less than 0.7% [2].

Uncertainty in the measurement of the wind speed in the LSWT test section is discussed in Appendix A.

## 2.2 Generic Submarine Model

The generic submarine model was designed and manufactured for testing in both the DSTO LSWT, and, with minor modification, a water tunnel. The model length (L) is 1.35 m and model diameter (D) is 0.185 m. The model is machined from aluminium and comprises a cylindrical centre-body with an ellipsoid nose and a streamlined tail section. When fully assembled the model has fineness ratio (L/D) of approximately 7.3. Nominally representative of a modern submarine shape, this generic test article has no full-scale equivalent.

### 2.2.1 Model Configuration

In this study the bare-hull configuration was tested and refers to the hull-form of the generic submarine model with no appendages attached, i.e. the casing, fin and control surfaces were not fitted, as shown in Figure 1.

### 2.2.2 Support System

During these tests, the model was fitted with a 'dummy' balance and connected to a single vertical support pylon. A dummy balance was used in order to protect the operational strain gauge balance from the PIV seed particles. Figure 1 shows the model mounted on a pylon within the working section of the LSWT. The model pitch attitude was controlled via a trailing support-arm and vertical control link mechanism. The model pitch was measured by an inclinometer, Jewel Instruments LCF-300 unit, fitted inside the model. The vertical support pylon was shrouded by a detachable aerodynamic fairing, and mounted on a rotating turn-table allowing the model to be yawed relative to the freestream flow. The model yaw attitude was measured by the turn-table encoder. The inclinometer pitch angle bias and precision uncertainty is  $\pm 0.029^\circ$  and  $\pm 0.023^\circ$ , respectively [1]. For the turn-table encoder the yaw angle uncertainty is  $\pm 0.1^\circ$  [1].

### 2.2.3 Blockage Ratio

The overall frontal area blockage ratio for the model at zero-incidence was estimated to be 2.1% of the test section cross-sectional area. This value represents the sum of the frontal area of the model (i.e. 0.5%) and the pylon fairing (i.e. 1.6%).



Figure 1 – Generic submarine model mounted in the LSWT

#### 2.2.4 Boundary Layer Transition

For all the experiments a boundary layer trip was employed. A 3 mm wide strip consisting of carborundum grit was attached circumferentially around the nose of the model at 5% of the body length. An empirical method, described in reference [3], was used to determine the appropriate grit size (i.e. size 80, or an average particle diameter of 0.21 mm) for this test programme. During the force and moment experiments a sound test (using a stethoscope traversed manually within the boundary layer) and a thermal imaging technique confirmed that this arrangement successfully transitioned the boundary layer to a turbulent state [1].

## 3. Experimental Method

### 3.1 Smoke Flow Visualisation

Smoke flow visualisation provided a qualitative assessment of the flow around the submarine model. An Aerotech Smoke Generator supplying Shell Ondina EL oil to a heated probe was used to generate the smoke. The probe was attached to the end of a long, slender rod that was used to position the smoke stream into the flow-field around the submarine model. The smoke flow patterns were simultaneously recorded on video at 1080i resolution using two Sony HXR-NX5P cameras from two orthogonal viewing

positions directly above and to the side of the test section. A Pelco standard definition observation camera located inside the tunnel, downstream of the model, also provided video recording. The observation camera and two Sony cameras were synchronised using a camera flash and matching the appropriate frame from each camera during post-processing.

Two Dedolight Universal Light Heads were used for lighting. The smoke stream and model were illuminated by positioning one of the light heads inside the test section downstream of the model with the light directed along the body axis of the model. In order to minimise shadows from the model and surface reflections back to the recording cameras, a second light head was positioned outside the test section, upstream of the model at approximately 45° to the oncoming flow. To improve the contrast of the smoke stream, the working section walls were covered with matte black paper.

### 3.2 Particle Image Velocimetry

PIV is a non-intrusive optical velocity measurement technique yielding planar whole field quantitative measurements of instantaneous and mean velocity. The technique is described schematically in Figure 2. The PIV technique requires the flow-field to be seeded with small particles which accurately follow the flow. A dual-pulse laser is used to illuminate a thin sheet of the flow with a short time delay,  $\Delta t$ , between the two pulses. The light scattered by the seed particles is recorded by a digital camera, in this case a camera with a frame-straddling CCD sensor, positioned normal to the laser sheet. By prescribing the time delay between pulses ( $\Delta t$ ) and measuring the particle displacement ( $\Delta x$ ) between the two recorded images, the velocity field can be computed as  $\Delta x/\Delta t$ . In practice the particle displacement is computed by dividing the recorded image into sub-areas called interrogation windows (IW). The in-plane displacement of the particles in each IW is obtained using statistical image cross-correlation. A velocity vector map over the whole image area is obtained by repeating the cross-correlation and velocity calculation for each IW. A detailed description of the PIV technique is given in [4].

In this study the 2D plane of interest was illuminated using a New Wave Solo PIV 200XT Nd:YAG dual laser-head. This laser emits two independently controlled beams at a wavelength of 532 nm, a maximum pulse energy of 200 mJ and a 5 ns pulse width. The laser was mounted above the wind tunnel test section on a two degree of freedom translating system as illustrated in Figure 3. The laser traverse was designed using MiniTec components. An optical train comprising a cylindrical and spherical lens was used to generate the light sheet. The laser sheet was aligned along the model centre-line and parallel to the flow direction, as shown in Figure 3. In order to minimise laser reflection towards the CCD camera, it was necessary to shift the laser sheet by 1 mm in the positive z-direction (away from the camera). On the surface of the model the laser sheet was measured to be 1.5 mm thick.

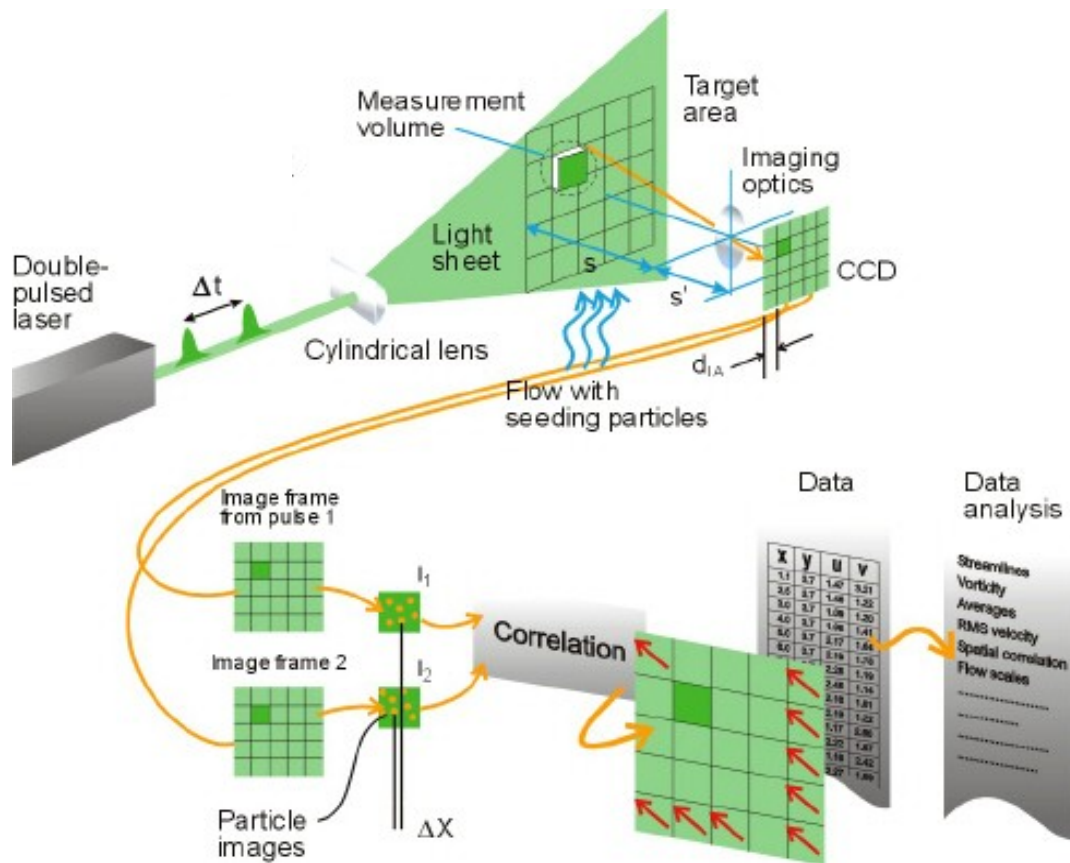


Figure 2 – PIV measurement principle (image from Dantec Dynamics [5])

The PIV image acquisition system consisted of a TSI PowerView™ Plus 11 megapixel CCD camera, fitted with a 200 mm Micro Nikkor f/4 lens. The CCD camera has a pixel resolution of  $4008 \times 2672$ , a pixel size of  $9 \mu\text{m} \times 9 \mu\text{m}$  and a frame rate of 2.07 Hz in frame straddling mode. Data acquisition and processing of the instantaneous flow-field images was achieved using the TSI INSIGHT™ 3G software. Ensemble averaging of the instantaneous vectors fields and further post-processing was then performed using a Matlab program developed in-house. The camera was mounted on a three degree of freedom translating system and was positioned orthogonal to the laser sheet, as shown in Figure 3. The camera traverse comprised of Thorlabs XT95 rail series and custom built components.

The PIV seed particles comprised of olive oil droplets generated through a Laskin nozzle (TSI 6-jet oil droplet generator) which was connected to a compressed air supply and remotely controlled using a solenoid valve. The wind tunnel circuit was seeded globally with the oil aerosol introduced downstream of the model. The particles have a specific gravity of approximately 0.92, a mean diameter of approximately  $1 \mu\text{m}$ , and a particle relaxation time which was calculated to be approximately  $2.4 \mu\text{s}$ .

### 3.2.1 Axes System

The axes system used for the PIV measurements is defined in Figure 3, with the origin located at the tail of the submarine model. The local coordinate system is defined with the x-direction in-line with the positive freestream direction, positive y-direction is upwards and the z-direction is positive starboard.

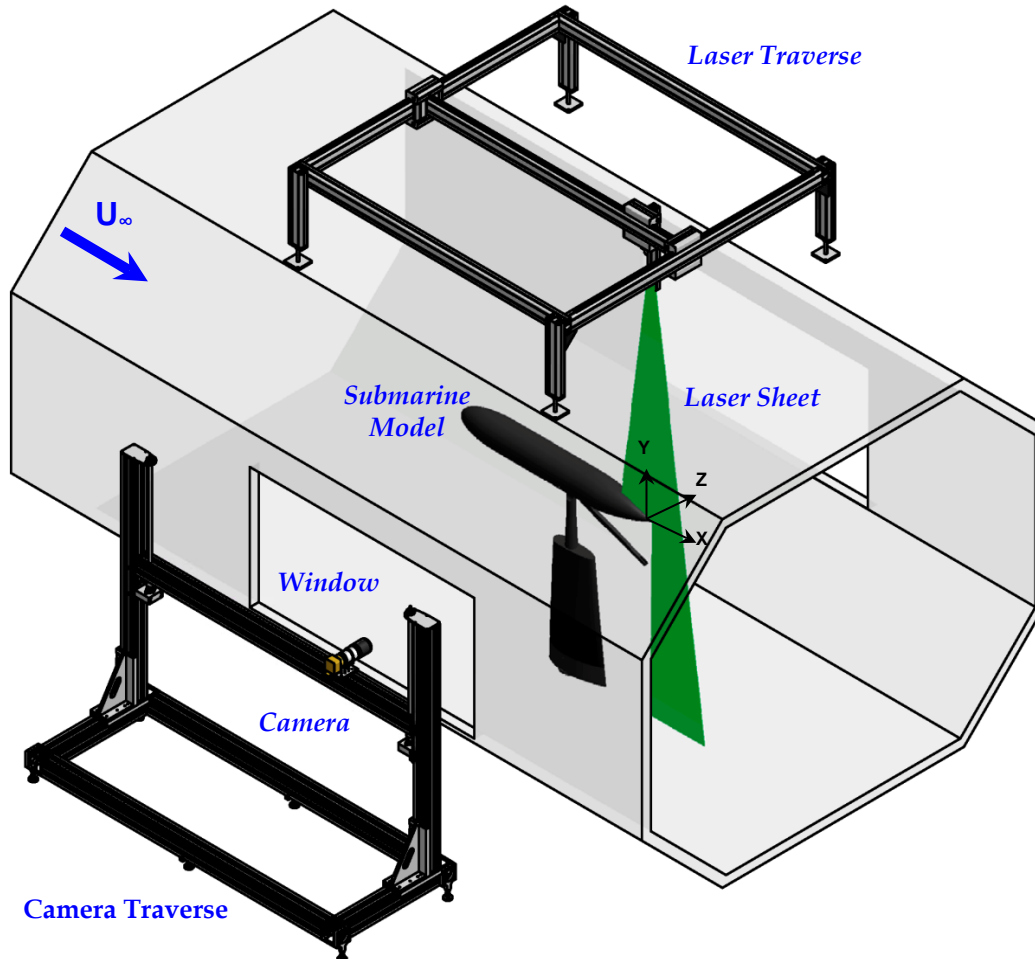


Figure 3 – PIV arrangement with the model mounted in LSWT

### 3.3 Derived Quantities

Large quantities of velocity field data generated from the PIV measurements allow a number of important flow quantities to be calculated, such as spatial velocity gradients, out-of-plane vorticity and Reynolds stresses. The velocity data is two-dimensional in nature and has a temporal functional dependence, consequently derived quantities also contain a spatial dependence in two-dimensions and a temporal dependence. A detailed uncertainty analysis of each flow quantity is described in Appendix C.

### 3.3.1 Velocity

In the current investigation, experiments were performed in the x-y plane (see Figure 3). From the in-plane displacements,  $\Delta X$  and  $\Delta Y$ , calculated from the PIV images, the fluid velocity,  $u$  and  $v$  at a point in the flow,  $x, y$  and at time,  $t$ , may be obtained by,

$$u(x, y, t) = \frac{\Delta X \times M}{\Delta t}$$

and

$$v(x, y, t) = \frac{\Delta Y \times M}{\Delta t}, \quad (3.1)$$

where  $\Delta t$  is the time separation between successive images pairs and  $M$  is the image magnification. Applying Eq 3.1 for each IW within a PIV image pair results in an instantaneous two-dimensional velocity field.

### 3.3.2 Mean Velocity

Analysis of turbulent flow data, or any random flow data, requires the definition of an averaging operator for the experiment. The ideal average is the ensemble average, which is defined as the mean over an infinite collection of realisations [6]. A flow field is said to be statistically stationary in time if the ensemble averages of all properties are independent of time [6]. For the current PIV experiments the flow is assumed statistically stationary in time and the camera is triggered to take samples of the velocity field periodically in time. The time between successive frame pairs (here  $\sim 0.5$  seconds) is also assumed large enough so that successive measurements are statistically uncorrelated. An ensemble average is then approximated by summing over a large, but finite collection of these samples ( $N$ ). It is assumed that the ensemble average in this experiment is equal to the time average and consequently the ensemble average for infinite samples. The effect of the number of PIV samples used to estimate the ensemble average in terms of the sampling uncertainty, or uncertainty in the mean, is discussed in Appendix C.

The mean velocity at a point in the flow,  $x, y$ , calculated from  $N$  velocity realisations is defined as,

$$\bar{u}(x, y) \equiv \langle u(x, y, t) \rangle = \frac{1}{N} \sum_{n=1}^N u(x, y, t_n), \quad (3.2)$$

where  $\langle \cdot \rangle$  denotes the expected value (or ensemble average) over  $N$  realisation. The mean velocity components calculated from the PIV measurements are therefore,

$$\bar{u}(x, y), \bar{v}(x, y). \quad (3.3)$$

### 3.3.3 Vorticity and Velocity Gradients

The measurement of the velocity components in Eq. (3.2) allowed the calculation of the out of plane vorticity component,

$$\omega_z(x, y, t) = \frac{\partial v}{\partial x} - \frac{\partial u}{\partial y}. \quad (3.4)$$

The vorticity was derived by calculating the spatial velocity derivatives  $(\frac{\partial v}{\partial x}, \frac{\partial u}{\partial y})$  using a second-order central finite difference scheme at the interior points,

$$\frac{\partial f}{\partial x} = \frac{f(i-1) - f(i+1)}{2\Delta}, \quad (3.5)$$

where  $f$  is generic function and  $i$  is the spatial coordinate index in the  $x$  direction.

The second order forward difference,

$$\frac{\partial f}{\partial x} = \frac{-3f(i) + 4f(i+1) - f(i+2)}{2\Delta}, \quad (3.6)$$

and backward difference,

$$\frac{\partial f}{\partial x} = \frac{f(i-2) - 4f(i-1) + 3f(i)}{2\Delta}, \quad (3.7)$$

schemes were used at the boundary of the region of interest. For interior points coinciding with spurious data, second-order finite difference could not be used, and instead a second-order forward or backward difference was used. Spurious data is discussed in Section 3.4. Etabari and Vlachos [7] indicate that the second-order central finite difference scheme gives the best trade-off in performance between the associated bias and precision uncertainty resulting from a particular computational method used to calculate the velocity derivatives.

### 3.3.4 Mean Vorticity

The mean vorticity at a point in the flow,  $x, y$ , calculated from  $N$  velocity realisations is defined as,

$$\overline{\omega_z}(x, y) \equiv \langle \omega_z(x, y, t) \rangle. \quad (3.8)$$

### 3.3.5 Turbulent Quantities

The velocity fluctuating components were determined as follows,

$$u'(x, y, t) = u(x, y, t) - \overline{u}(x, y), \quad (3.9)$$

$$v'(x, y, t) = v(x, y, t) - \overline{v}(x, y). \quad (3.10)$$

The in-plane Reynolds stress at a point in the flow,  $x, y$ , calculated from  $N$  velocity realisations is defined as,

$$\overline{u'^2}(x, y) \equiv \left\langle \left( u(x, y, t) - \bar{u}(x, y) \right) \left( u(x, y, t) - \bar{u}(x, y) \right) \right\rangle. \quad (3.11)$$

The other Reynolds stress components ( $\overline{v'^2}(x, y)$  and  $\overline{u'v'}(x, y)$ ) can similarly be obtained. The turbulence strength or root-mean-square of the velocity fluctuation is

$$u_{RMS}(x, y) = \sqrt{\overline{u'^2}(x, y)}, \quad (3.12)$$

and the turbulence intensity,

$$u_{RMS}(x, y) / U_{\infty}. \quad (3.13)$$

Similarly the v-component turbulence strength and turbulence intensity are defined as,

$$v_{RMS}(x, y) = \sqrt{\overline{v'^2}(x, y)}, \text{ and } v_{RMS}(x, y) / U_{\infty}. \quad (3.14)$$

### 3.4 Data Processing and Validation Criteria

The particle displacements are derived by processing the PIV image pairs using the Insight 3G software. Within each IW the particle displacement are computed using a two-pass recursive algorithm with an IW size for both the first and second pass of  $64 \times 64$  pixels and a 50% grid spacing overlap. Each vector in the resultant vector field was then validated and filtered to eliminate spurious (or invalid) vectors which may be the result of low particle seeding, strong velocity gradients, particles moving out-of-plane due to three-dimensional motion or a noisy image. This comprised a global velocity range filter, a mean filter using a neighbourhood size of  $3 \times 3$  pixels and a displacement tolerance of 2 pixels. Vectors identified as invalid were then replaced with interpolated points using bi-linear interpolation.

Liang *et al.* [8] state that for well-optimised PIV experiments, the spurious vector count should be less than 5% of the total number of measured vectors. In this study if a single velocity vector field contained spurious vector numbers greater than 5% of the total number of measured vectors it was not included in the ensemble average. This resulted in some of the mean flow-fields being averaged over less than the number of acquired images. The final number of samples ( $N$ ) used in the ensemble average for each test case is listed in Table 2. Whilst some test cases had fewer samples than 1000, in Section 4.4.2, a sample size of 500 is shown to be sufficient for the convergence of mean flow and turbulent parameters.

In some cases the PIV measurement fields contained regions of invalid data located in the same region for each field. Where possible these regions were masked out leaving only the valid PIV data. Further discussion regarding the factors contributing to invalid data regions are presented in Section 4.5. After post processing the PIV data, three test cases were discarded as they were found to have a significant amount (>10%) of spurious vectors present in each field. Of the remaining valid fields, statistical analysis revealed that the mean number of spurious vectors in a single processed PIV image was less than 1.6% and 95% of the fields contained less than 2.8% spurious vectors. Thus for the majority of test cases, the PIV measurements were of a high quality.

### 3.5 Test Conditions

The generic submarine model was tested at various angles-of-attack ( $\alpha$ ) and angles-of-sideslip ( $\beta$ ). The freestream airspeed ( $U_\infty$ ) in the wind tunnel was dictated by the experimental technique used. The smoke flow visualisation technique required lower speeds so that the smoke stream did not disperse too quickly, whereas for the PIV measurement higher speeds could be attained.

The smoke flow visualisation tests were conducted at  $U_\infty = 5$  m/s and the following model orientations:

- Pitch,  $\alpha = 0^\circ, \pm 2.5^\circ, \pm 5^\circ, \pm 10^\circ$  and  $\pm 15^\circ$  (at zero yaw)
- Yaw,  $\beta = 0^\circ, 5^\circ, 10^\circ, 20^\circ$  and  $30^\circ$  (at zero pitch)
- Combined pitch and yaw of  $-15^\circ$  pitch/ $15^\circ$  yaw and  $15^\circ$  pitch/ $30^\circ$  yaw.

The test matrix for the PIV tests is shown in Table 1. The majority of the PIV measurements were conducted at  $U_\infty = 30$  m/s. The effect of Reynolds number based on the model length ( $Re_L = \rho U_\infty L / \mu$ ), was studied by performing PIV measurements at  $U_\infty = 20$  m/s, 30 m/s and 40 m/s for the model at  $\alpha = 0^\circ$  and  $\beta = 0^\circ$ .

Table 1 – PIV test matrix

$\alpha$ ( $^\circ$ )	$U_\infty$ (m/s)	$Re_L$
0	20	$1.8 \times 10^6$
2.5, 0, -2.5, 5, 10, 15	30	$2.7 \times 10^6$
0	40	$3.6 \times 10^6$

The PIV test conditions and associated PIV parameter settings are defined in Table 2. The field-of-view column refers to the discrete locations on the model where measurements were taken and are detailed in Section 3.6. The time intervals between laser pulses ( $\Delta t$ ) were based on a requirement that the maximum particle displacements be less than 25% of the  $64 \times 64$  pixel IW. Three test cases were discarded due to large percentage of spurious vectors (see Section 3.4). A summary of the PIV measurement settings is provided in Appendix B.

Table 2 – PIV test conditions and flow measurement parameters at different pitch angles at zero yaw

Field-of-view	$\alpha(^{\circ})$	$U_{\infty}$ (m/s)	$\Delta t$ ( $\mu$ s)	Number of fields (N)
1	-2.5	29.9	10	1000
2	-2.5	29.9	10	1000
3	-2.5	29.9	10	1000
1	0	19.8	15	960
1	0	40.5	6	906
1	0	30.4	10	827
2	0	30.2	10	1000
3	0	30.0	10	discarded
1	2.5	30.3	10	910
2	2.5	30.3	10	1000
3	2.5	29.9	10	1000
1	5	29.9	10	1000
2	5	29.9	10	discarded
3	5	29.9	10	1000
1	10	29.9	10	1000
2	10	29.9	10	999
3	10	29.9	10	1000
1	15	30.0	10	986
2	15	30.3	13	discarded
3	15	30.3	13	1000

### 3.6 Particle Image Velocimetry Measurement Locations

The image field-of-view is the visible extent of the flow field captured on the camera sensor. It is desirable for the field-of-view to be sufficiently large so as to capture the entire region of interest in a single realisation. Conversely, high spatial resolution is required in order to adequately resolve flow features around the model. These requirements are conflicting, since a high spatial resolution results in a smaller field-of-view.

In addition to the above constraints, another important PIV requirement is to avoid peak-locking (also known as pixel-locking). Peak-locking is the tendency of PIV measurements to bias towards integer displacements. This occurs when the particle images are under-resolved and the peak fit applied to the cross-correlation function (a three-point Gaussian) is unable to accurately determine the correlation peak to sub-pixel accuracy [9]. For a three-point Gaussian peak fit applied to the cross-correlation function, the optimum particle image diameter for PIV measurements is between 2 to 3 pixels [4]. Practically in this test, such a particle image diameter was not possible due to the following factors:

- the diameter of the olive oil droplets were small (nominally 1  $\mu$ m),
- the image magnification was limited as the camera was located relatively far from the object measurement plane, and
- the maximum focal length lens available was a 200 mm Micro-Nikkor.

A typical approach to improve the particle image size is to increase the camera lens f-stop, which increases the diffraction limited particle diameter. The drawback with this approach is that, in order to maintain the same exposure, each increase in f-stop requires a doubling of laser light intensity. Alternatively, to achieve a larger image particle diameter (and higher spatial resolution) an imaging lens with a longer focal length could be used, but was not available for this experiment. Peak-locking for the current experiment is assessed in Section 4.4.3.

For this study, in order to image an overall larger area and have sufficient resolution to avoid peak-locking, three high resolution field-of-views were blended together. The distance from the centre of the test section to the PIV camera was approximately 1.6 m and using the 200 mm lens, a reproduction ratio (i.e. ratio of subject size on sensor plane to the actual subject size) of 6.67 resulted. The corresponding image spatial resolution was 60.03  $\mu\text{m}/\text{pixel}$  and the field-of-view for each image was 240 mm  $\times$  160 mm.

The PIV measurements were focused around the tail and wake region of the generic submarine model. The locations of the three field-of-views over which measurements were planned are shown in Figure 4. However, due to the optical distortions produced by the test section window (described in Section 4.5.2), these locations could not always be obtained for each measurement case. Overlapping the field-of-views allowed the data to be blended together during post-processing using the approach described in Kumar *et. al* [10]. The amalgamation of the three field-of-views is shown in Figure 5 with respect to the entire model body. Blending multiple high resolution fields is common practise in studies using PIV, and has been reported in submarine research [11].

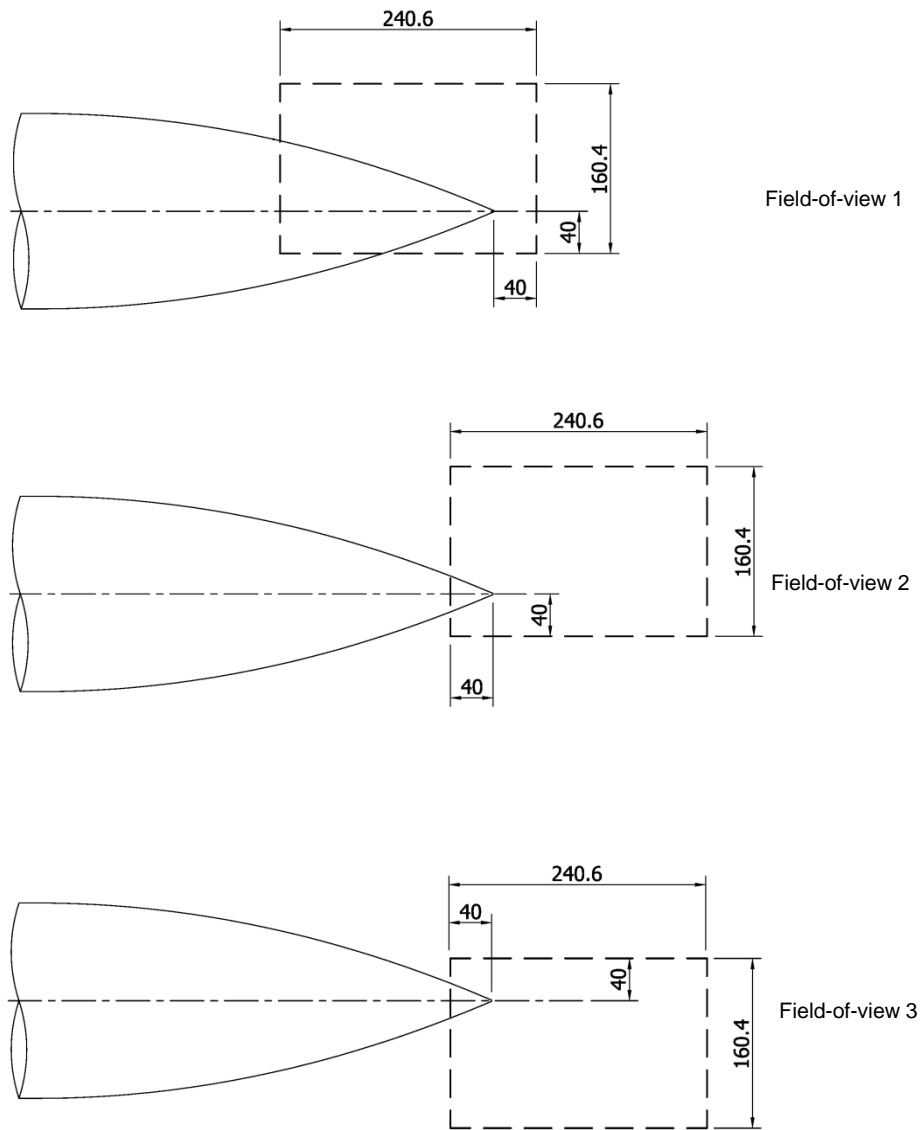


Figure 4 - The location and size of the three PIV field-of-views with respect to the model tail. (All dimensions are in mm.)

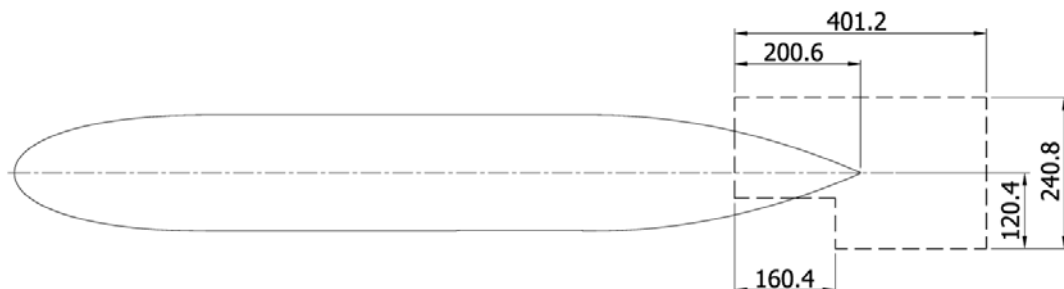


Figure 5 - The amalgamation of the three PIV field-of-views with respect to the model body. (All dimensions are in mm.)

## 4. Results

### 4.1 Smoke Flow Visualisation

Smoke visualisation provided qualitative insight into the flow around the submarine model and assisted in the interpretation of the PIV measurements. Figure 6 shows smoke flow visualisation patterns, on the starboard side of the model, with increasing  $\alpha$ . The inset image shows the camera view from above the test section taken at the same instance in time. At  $\alpha = 0^\circ$ , Figure 6(a) shows the flow is everywhere attached to the model. At  $\alpha = 2.5^\circ$ , the flow around the side of the hull remains attached and exhibits a small upward curvature. As  $\alpha$  is increased further, the curvature of the flow increases and begins further upstream. At  $\alpha = 5^\circ$ , there is evidence of separation at the tail. With increasing  $\alpha$ , this cross-stream separation migrates upstream. The resultant separated flow rolls up into a longitudinal vortex on each side of the body (as depicted schematically for a prolate spheroid in Figure 7). These longitudinal vortices are stronger and more pronounced as more smoke is entrained towards the core centre and the location where they detach from the body moves further upstream with increasing  $\alpha$ .

The flow patterns observed in the LSWT flow visualisation study of the hull body are consistent with studies of prolate spheroids of various axis ratios [12-16]. The flow around a prolate spheroid is characterised by cross-stream separation that forms on the tail at low  $\alpha$  and then migrates forward and leeward with increasing  $\alpha$ . The inward roll up of the longitudinal vortex, induces a downward velocity component along the vertical symmetry plane of the model (refer to Figure 7). As the model was pitched, this downward velocity component resulted in a centre-line flow which remained attached for all  $\alpha$  tested. An example of the attached flow along the vertical symmetry plane of the model is shown in Figure 8, for  $\alpha = 15^\circ$ . The two images are the same instance in time taken from the starboard side video camera and the observation camera inside the LSWT.

The generic submarine model in the bare hull configuration is axisymmetric, and in the absence of support interference effects,  $\beta$  is analogous to  $\alpha$ . This was evident in the smoke flow visualisation with the large-scale flow behaviour as  $\beta$  is increased. However, unlike pitch motion, increasing  $\beta$  showed the longitudinal vortices were present at an oblique angle. Due to the mounting arrangement, higher angles of  $\beta$  (up to  $30^\circ$ ) compared to  $\alpha$  could be achieved. At  $\beta = 30^\circ$  for example, Figure 9 show the smoke to be entrained in two distinct vortices which are approximately symmetric about the horizontal plane.

The smoke flow visualisation results clearly show the influence of the mounting arrangement, particularly on the underside of the model, toward the aft end. A turbulent wake downstream of the pylon-body junction was apparent, as well as flow separation and in some instances, vortex shedding. With the model at  $\alpha = 0^\circ$  and the smoke probe positioned in the aft fairing cut-out, a recirculation region was also evident and is shown in Figure 10. The flow around the fairing separates at the cut-out, and a portion of the flow enters the recirculation region. On exiting the recirculation region, the flow is disturbed by the pitch actuator arm. The flow interference effect appears to be greatest as the model is yawed. For large side-slip angles the pitch actuator arm is no longer in the pylon and fairing wake and becomes exposed to the oncoming flow. An example of vortex shedding from the pitch actuator arm, at  $\beta = 30^\circ$ , is shown in Figure 11. An unsteady flow-field

downstream of the vertical support pylon-model body junction was also observed in the wool tuft flow visualisation experiments performed by Quick *et al.* [1].

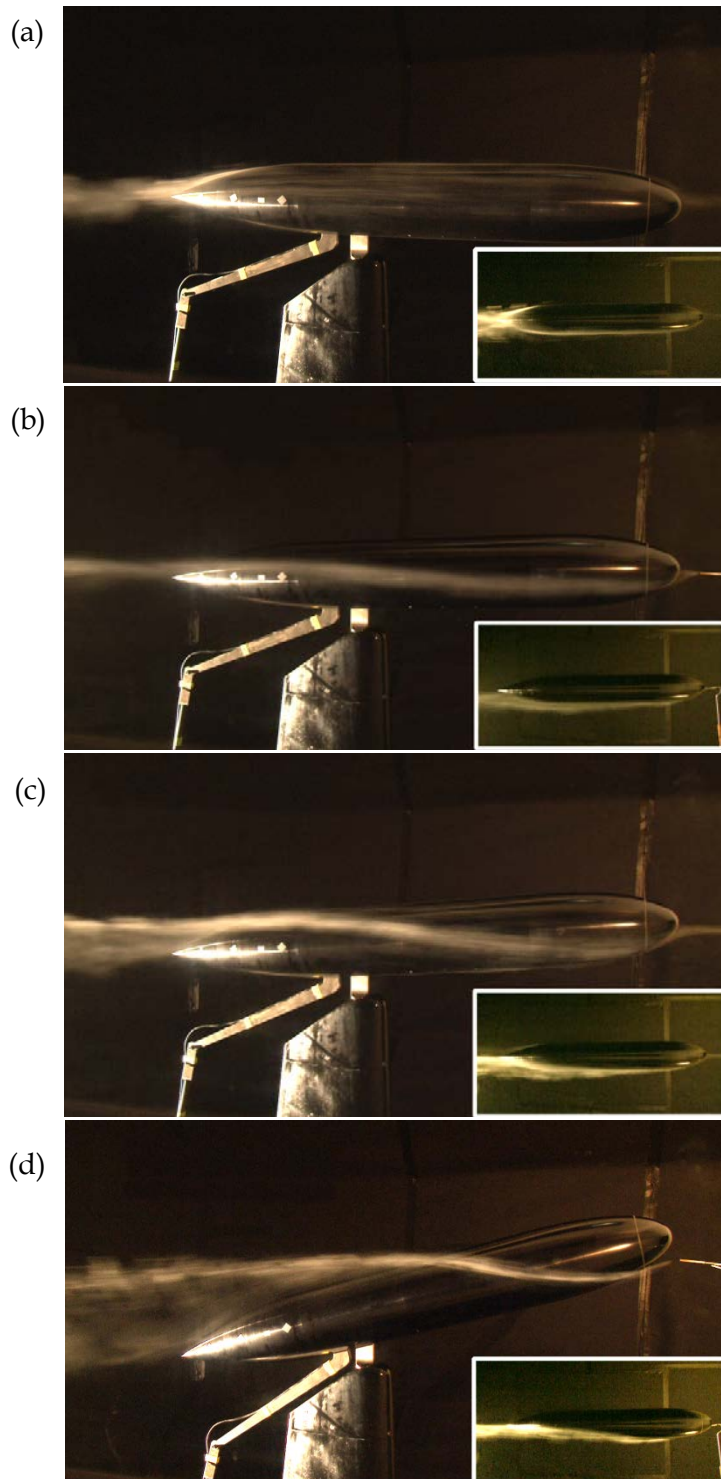


Figure 6 – Smoke flow visualisation patterns on the starboard side of the submarine model with increasing angle-of-attack (a)  $\alpha = 0^\circ$ , (b)  $\alpha = 2.5^\circ$ , (c)  $\alpha = 5^\circ$  and (d)  $\alpha = 15^\circ$

<sup>1</sup>Inset image show the view from above the model at the same instant in time.

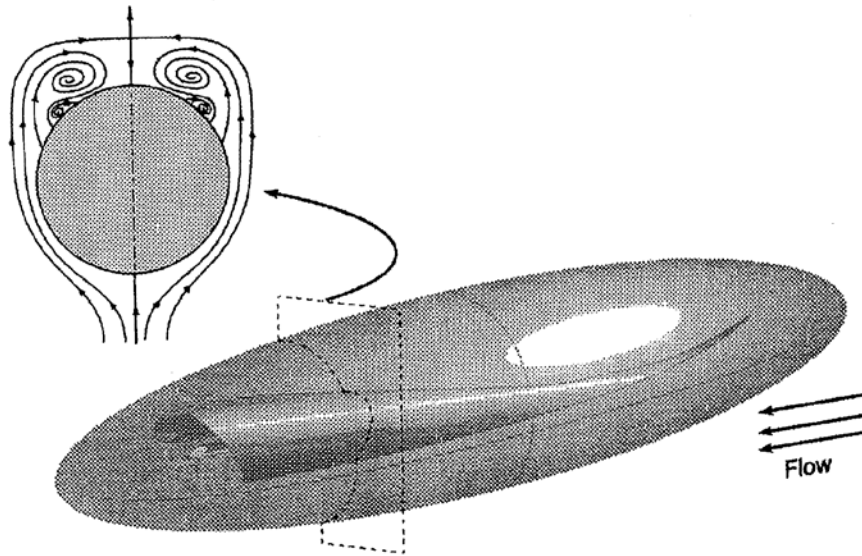


Figure 7 – Cross-flow separation on a prolate spheroid at pitch (from Chesnakas and Simpson [16])

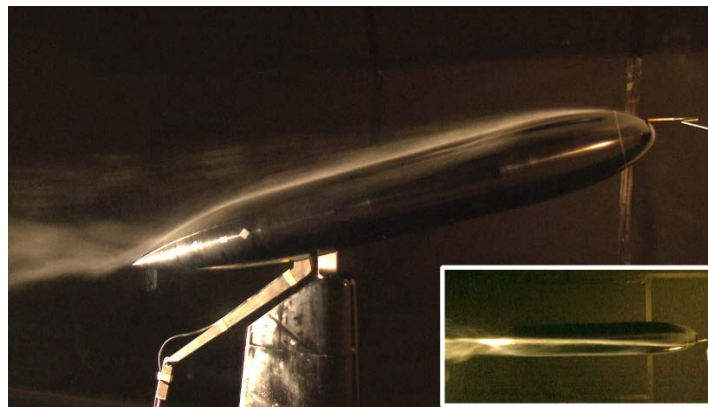


Figure 8 – Smoke flow visualisation at  $\alpha = 15^\circ$  and  $\beta = 0^\circ$ , showing attached flow along the centre-line of the model

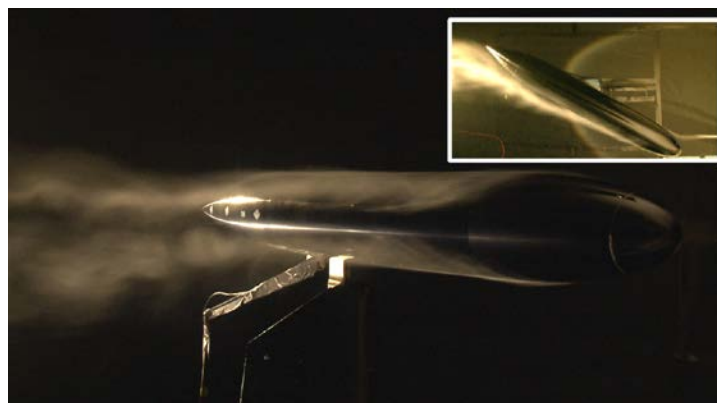


Figure 9 – Smoke flow visualisation at  $\alpha = 0^\circ$  and  $\beta = 30^\circ$ , showing roll-up of the vortex sheets into two distinct vortices



Figure 10 – Smoke flow visualisation at  $\alpha = 0^\circ$  and  $\beta = 0^\circ$ , with probe positioned at the aft fairing cut-out showing a recirculation region and an unsteady wake

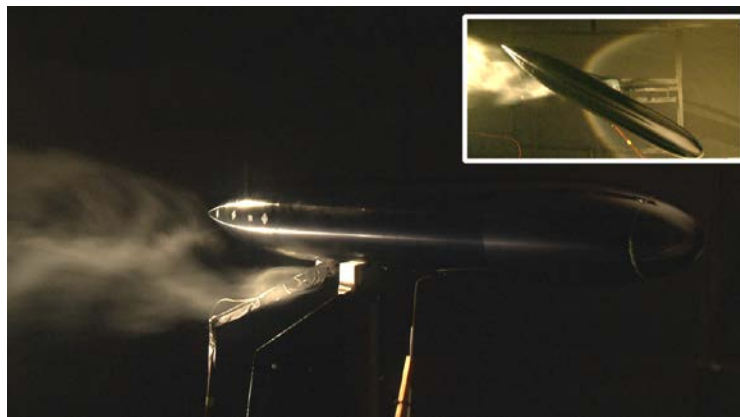


Figure 11 – Smoke flow visualisation at  $\alpha = 0^\circ$  and  $\beta = 30^\circ$ , showing vortex shedding from the pitch actuator arm

## 4.2 PIV Mean Flow-field

The mean PIV flow-field results were obtained by an ensemble average of the instantaneous vector fields over the number of samples taken for each case,  $N$ , as summarised in Table 2 in Section 3.5.

### 4.2.1 Flow-field at Low Angles-of-Attack

For  $\alpha = 0^\circ$ , Figure 12(a) shows the non-dimensional streamwise velocity field ( $\bar{u}/U_\infty$ ), together with the streamline pattern. Attached flow passes over the tail surface of the submarine model with the streamlines showing a small downward velocity component. The out-of-plane non-dimensional vorticity ( $\overline{\omega_z}L/U_\infty$ ) is presented in Figure 12(b). The boundary layer vorticity expands perpendicular to the model surface with downstream distance and forms a free shear layer beyond the tail. The region of higher vorticity

extends further downstream with decreasing  $\alpha$ . The Reynolds stress ( $-\overline{u'v'}/U_\infty^2$ ) contours are presented in Figure 12(c). The Reynolds stress plot displays the level of turbulence present in the flow, and shows strong intensities at the upstream end of the field-of-view and in the free wake region. It should be noted that in this and all other Reynolds stress contour plots presented, the magnitude of the Reynolds stress fluctuations are low compared to the experimental uncertainty (see Appendix C). The Reynolds stress contour plots therefore only provide a qualitative assessment of the flow. Strategies on how to reduce the PIV measurement uncertainty are described in Section 4.4.1.

The PIV results at  $\alpha = \pm 2.5^\circ$  display similar features to  $\alpha = 0^\circ$  and are shown in Figure 13 and Figure 14. In both cases, the boundary layer over the tail surface remains attached, with the stagnation point located at the model trailing edge. At  $-2.5^\circ$  the vorticity over the top of the model displays greater intensity, while at  $+2.5^\circ$  it is more diffuse. In the absence of model support interference effects, the flow features at  $\alpha$  of  $+2.5^\circ$  and  $-2.5^\circ$  should be a mirrored image about the  $y/L = 0$  line. However, both exhibit increased levels of turbulence in the lower wake region due to the flow unsteadiness generated by the vertical support pylon as identified in the flow visualisation.

#### 4.2.2 Flow-field at High Angles-of-Attack

The PIV results as the model is pitched at  $5^\circ$ ,  $10^\circ$  and  $15^\circ$  are shown in Figure 15, Figure 16 and Figure 17, respectively. With increasing  $\alpha$ , the streamlines over the top of the model are vectored down along the surface. This is consistent with the flow visualisation results at these  $\alpha$ , two longitudinal vortices roll up inward towards the surface of the model and induce a downward velocity along the vertical symmetry plane of the model. This downwash is also depicted in Figure 7 and is shown by the half-saddle in cross-section. For the tested  $\alpha$ , this downward velocity ensures the flow remains attached along the vertical symmetry plane of the model.

The vorticity contours show that, as  $\alpha$  increases from  $5^\circ$  to  $10^\circ$ , the boundary layer vorticity on the upper surface extends further downstream. With increasing  $\alpha$  the shear layer vorticity is “compressed” closer to the boundary of the model. At  $\alpha = 10^\circ$  and  $15^\circ$ , a thin streak of positive vorticity is also evident above the model, displaced from the model surface at  $\sim y/L = 0.08$ . Since the flow visualisation at these  $\alpha$  confirmed the presence of cross-stream separation and a flow topology similar to the sketch in Figure 7, this streak may be an artefact produced by the local junction flow between the counter-rotating vortices (i.e. the off-body node line) near the model symmetry plane.

The Reynolds stress contour plots show streamwise structures which become more concentrated with increasing  $\alpha$ .

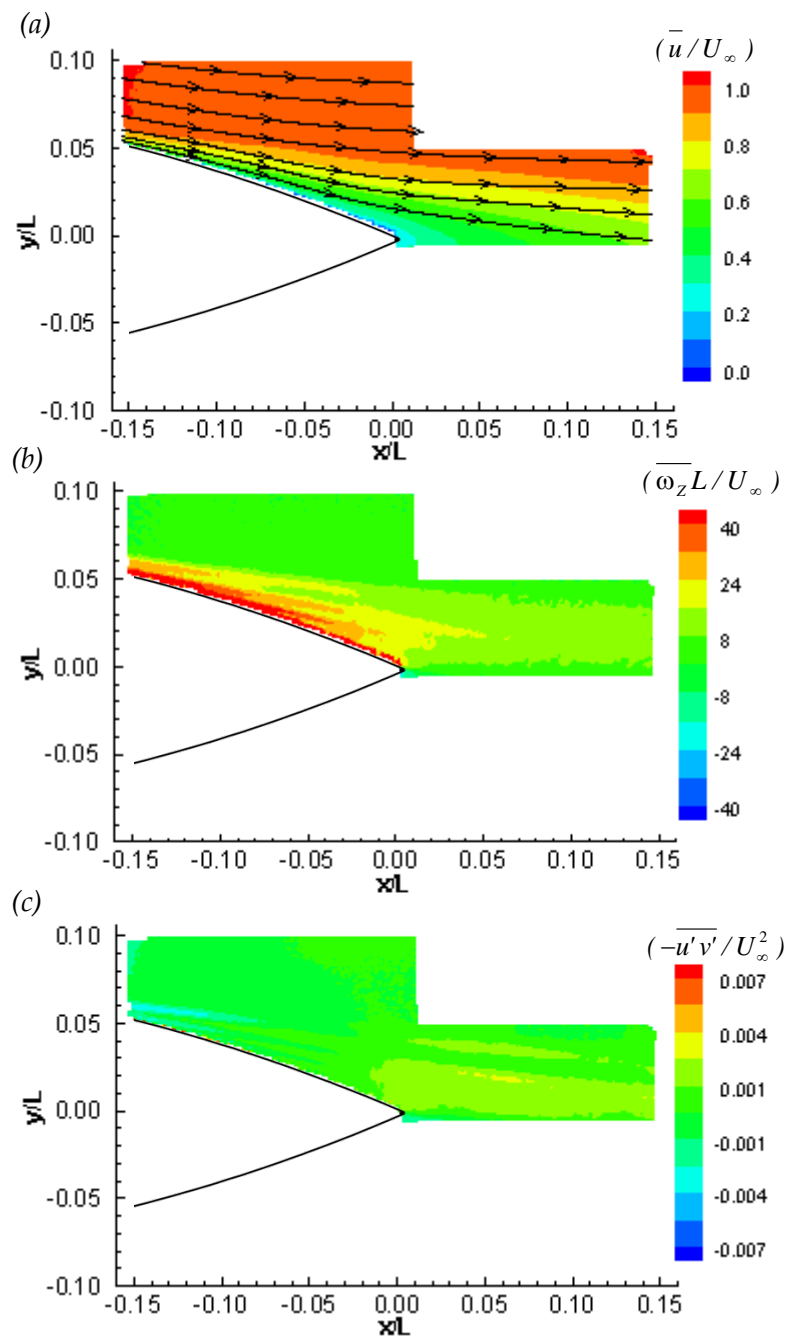


Figure 12 – (a) Streamline topology overlaid with non-dimensional streamwise velocity, (b) non-dimensional out-of-plane vorticity, (c) Reynolds stress contours at  $\alpha = 0^\circ$

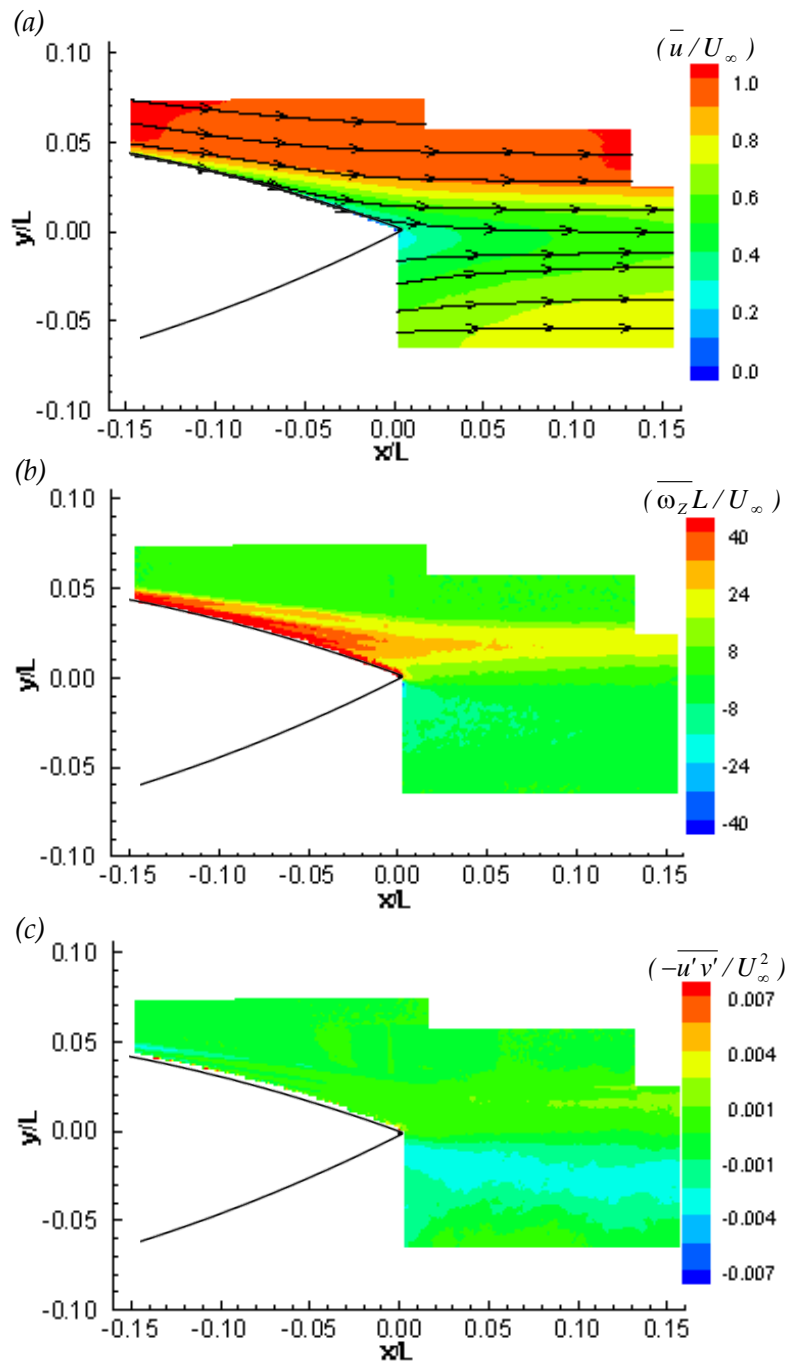


Figure 13 – (a) Streamline topology overlaid with non-dimensional streamwise velocity, (b) non-dimensional out-of-plane vorticity, (c) Reynolds stress contours at  $\alpha = -2.5^\circ$

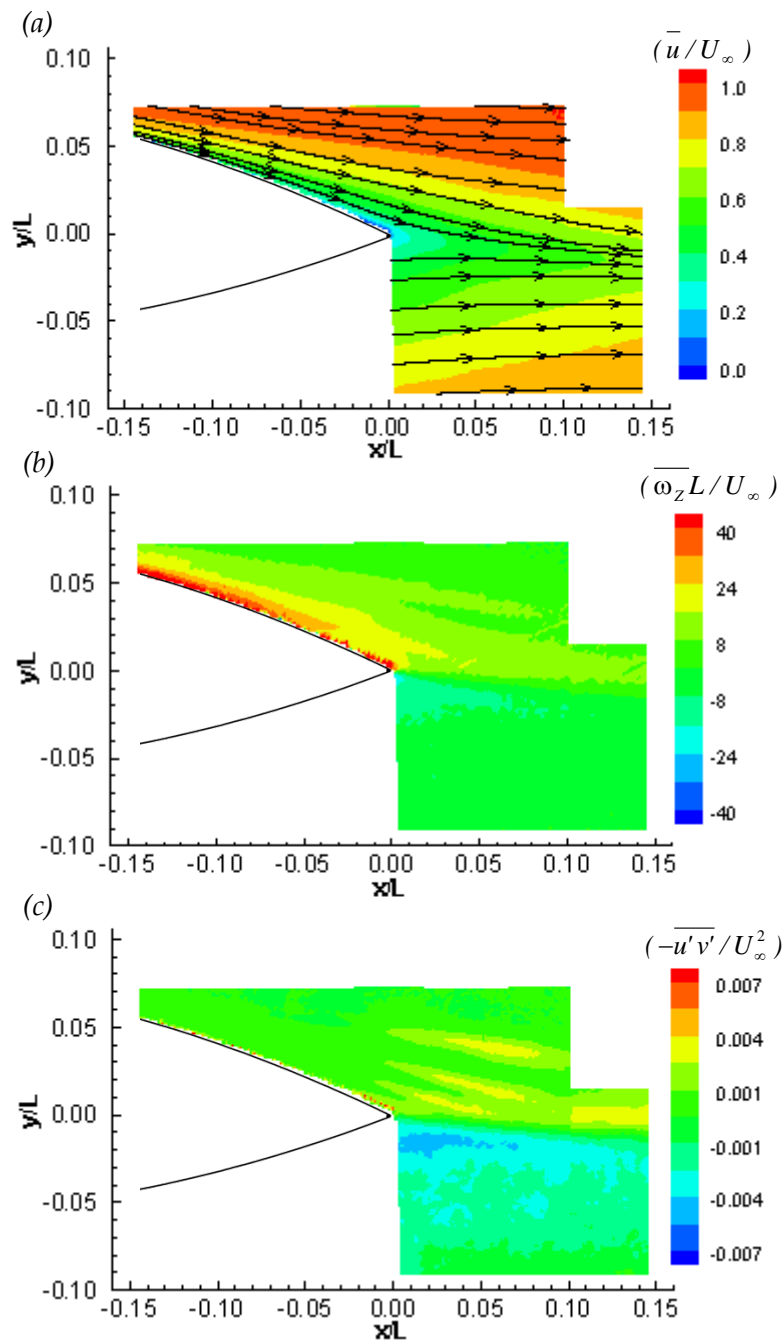


Figure 14 – (a) Streamline topology overlaid with non-dimensional streamwise velocity, (b) non-dimensional out-of-plane vorticity, (c) Reynolds stress contours at  $\alpha = 2.5^\circ$

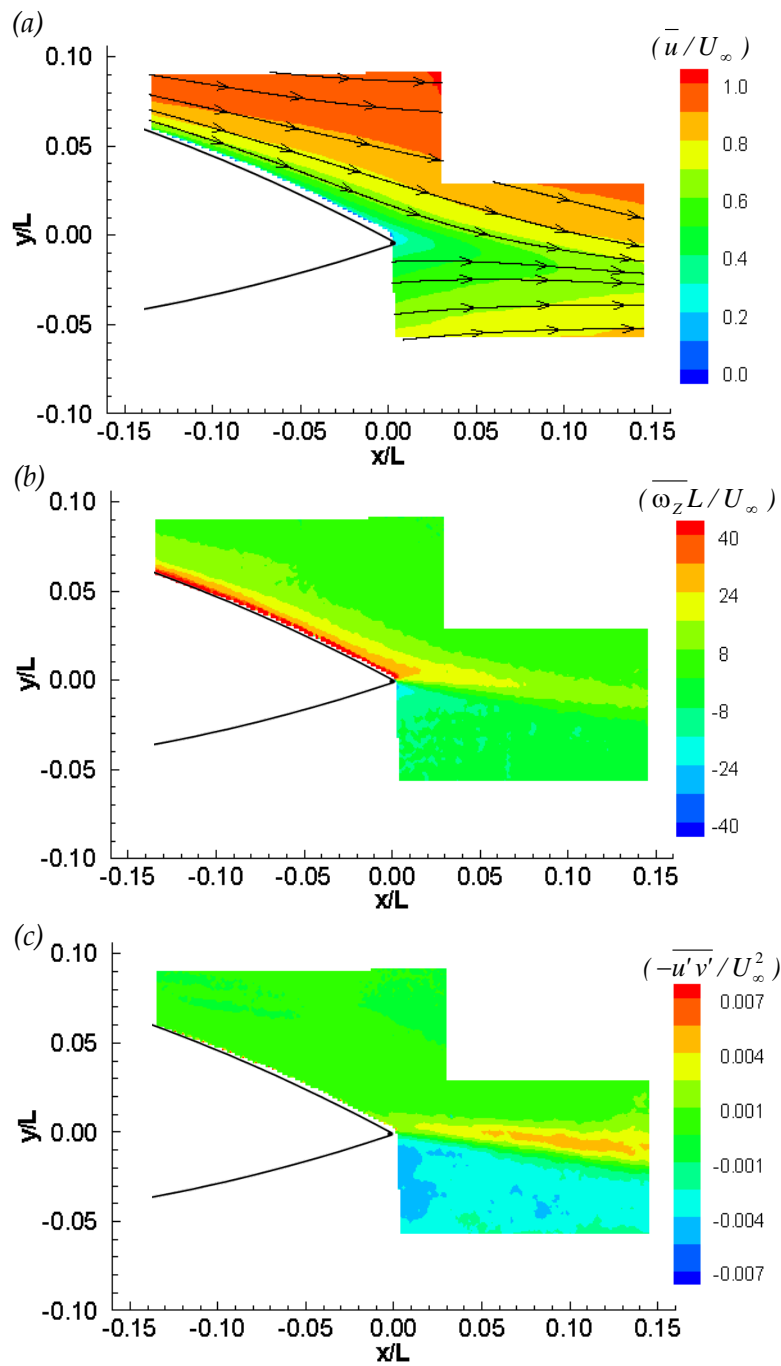


Figure 15 – (a) Streamline topology overlaid with non-dimensional streamwise velocity, (b) non-dimensional out-of-plane vorticity, (c) Reynolds stress contours at  $\alpha = 5^\circ$

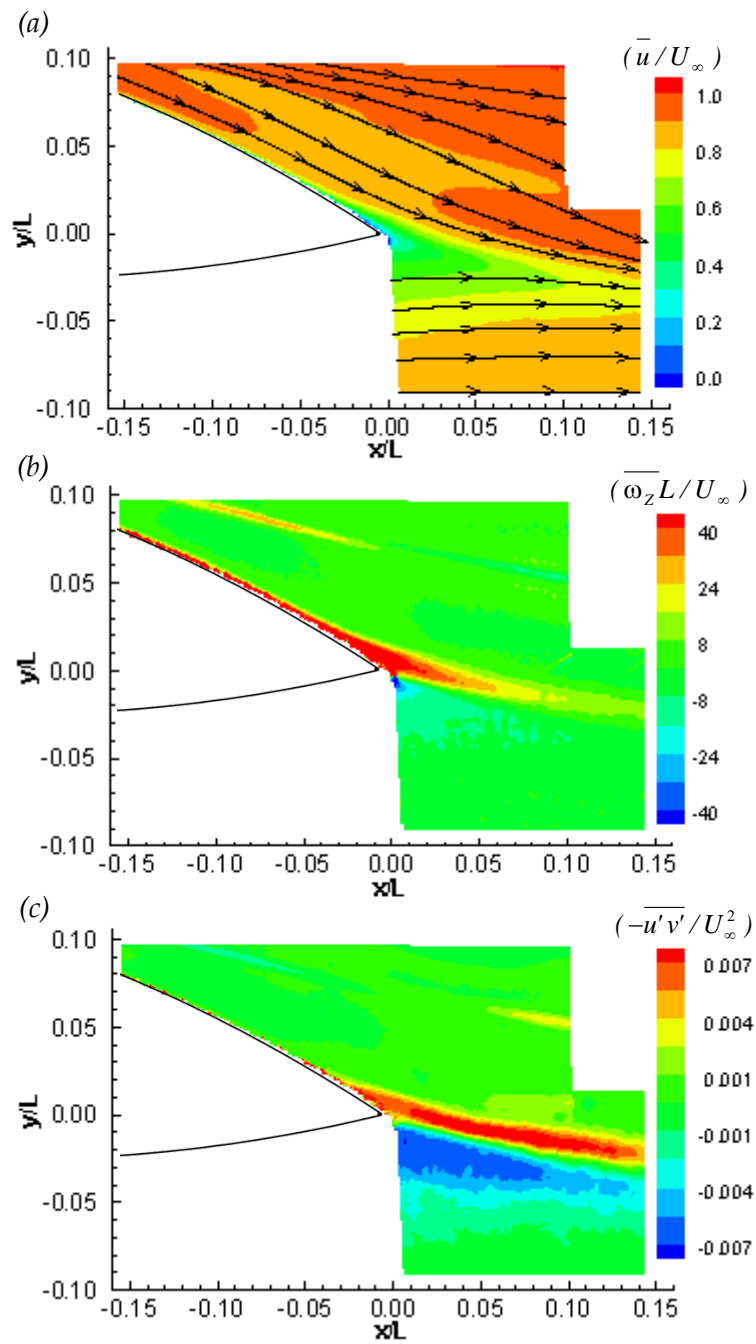


Figure 16 – (a) Streamline topology overlaid with non-dimensional streamwise velocity, (b) non-dimensional out-of-plane vorticity, (c) Reynolds stress contours at  $\alpha = 10^\circ$

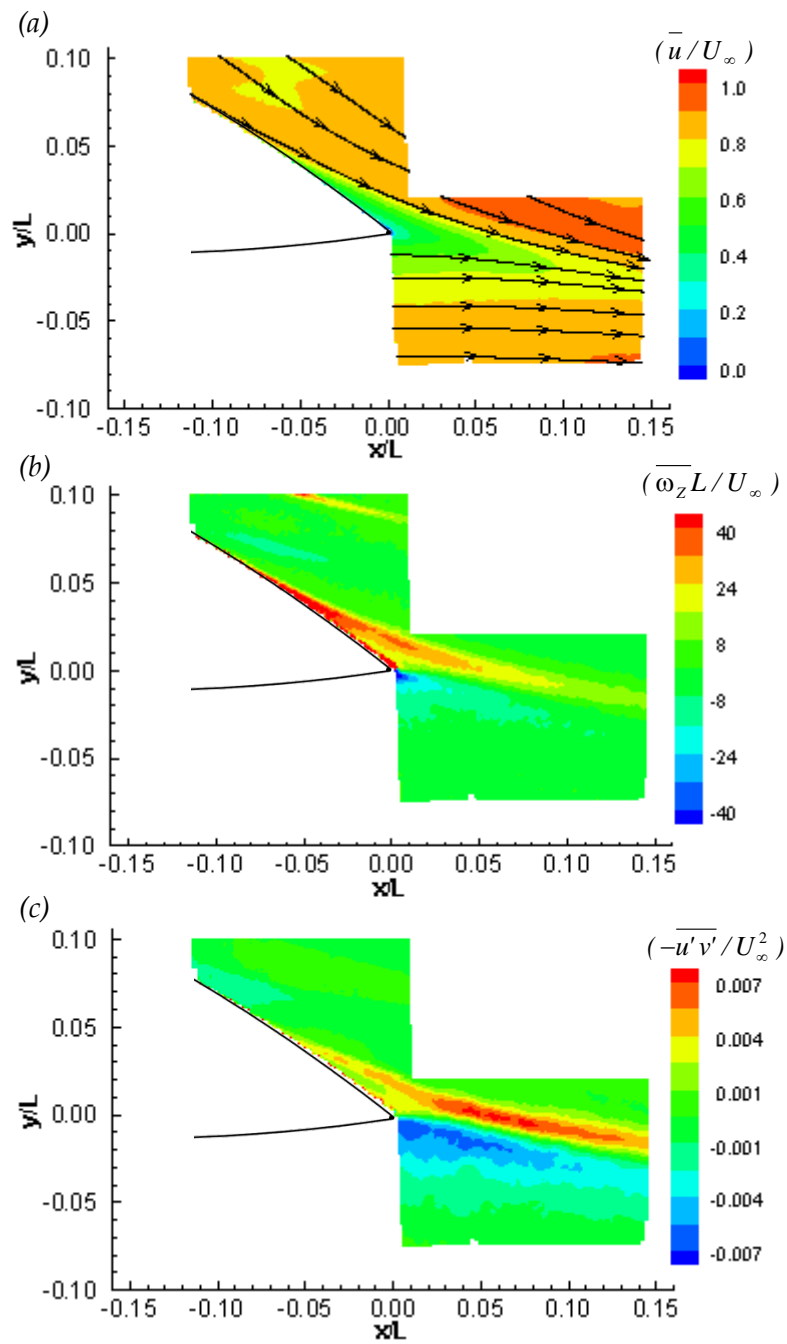


Figure 17 – (a) Streamline topology overlaid with non-dimensional streamwise velocity, (b) non-dimensional out-of-plane vorticity, (c) Reynolds stress contours at  $\alpha = 15^\circ$

### 4.2.3 Reynolds Number Sensitivity Study

A Reynolds number sensitivity study was conducted at  $\alpha = 0^\circ$  and for field-of-view 1 (see Figure 4). Freestream velocities of 20 m/s, 30 m/s and 40 m/s were tested, which correspond to Reynolds numbers, based on the model length, of  $1.8 \times 10^6$ ,  $2.7 \times 10^6$  and  $3.6 \times 10^6$ , respectively. The non-dimensional streamwise velocity contours, the out-of-plane non-dimensional vorticity and the Reynolds stress contours are presented for each Reynolds number in Figure 18. The flow field appears independent of  $Re_L$  for the range of velocities tested, as the contour plots for all three cases display similar flow patterns. An exception is the Reynolds stress plot for  $U_\infty = 40$  m/s, where two bands of concentrated negative Reynolds stress appear near the surface of the model and then dissipate with downstream distance. These low concentration bands are also evident in the vorticity contour plots and are more intense with increasing  $Re_L$ . It remains unclear if these bands are physical, due to the relatively high measurement uncertainty for these quantities. As discussed in Section 4.4.1, in the uncertainty in PIV measurements can be reduced by increasing the spatial resolution and increasing the sample size used in the ensemble average.

For this study there is a disparity between the Reynolds numbers in the smoke flow visualisation and PIV tests. The smoke visualisation testing was conducted at  $Re_L = 0.45 \times 10^6$ , whereas the PIV experiments were predominantly conducted at  $Re_L = 2.7 \times 10^6$ . In the case of flow over a prolate spheroid of axis ratio 6:1, it was discovered by Ahn [17] and then confirmed by Wetzel and Simpson [18], that a critical Reynolds number exists above which the flow-field is independent of the Reynolds number. They found that the cross-flow separation was insensitive to Reynolds number above  $Re_L = 2.5 \times 10^6$ . For the current study it is unclear if such a critical Reynolds number exists. The Reynolds number effect study was conducted at  $\alpha = 0^\circ$  and not at an incidence where the cross-stream separation is likely to be evident (i.e.  $\alpha > 5^\circ$ ). Further investigation is required in order to assess if a critical Reynolds number exists for the generic submarine shape tested here. Such investigations should utilise surface flow visualisation techniques as well as other test techniques which will enable the measurement of the cross-stream flows.

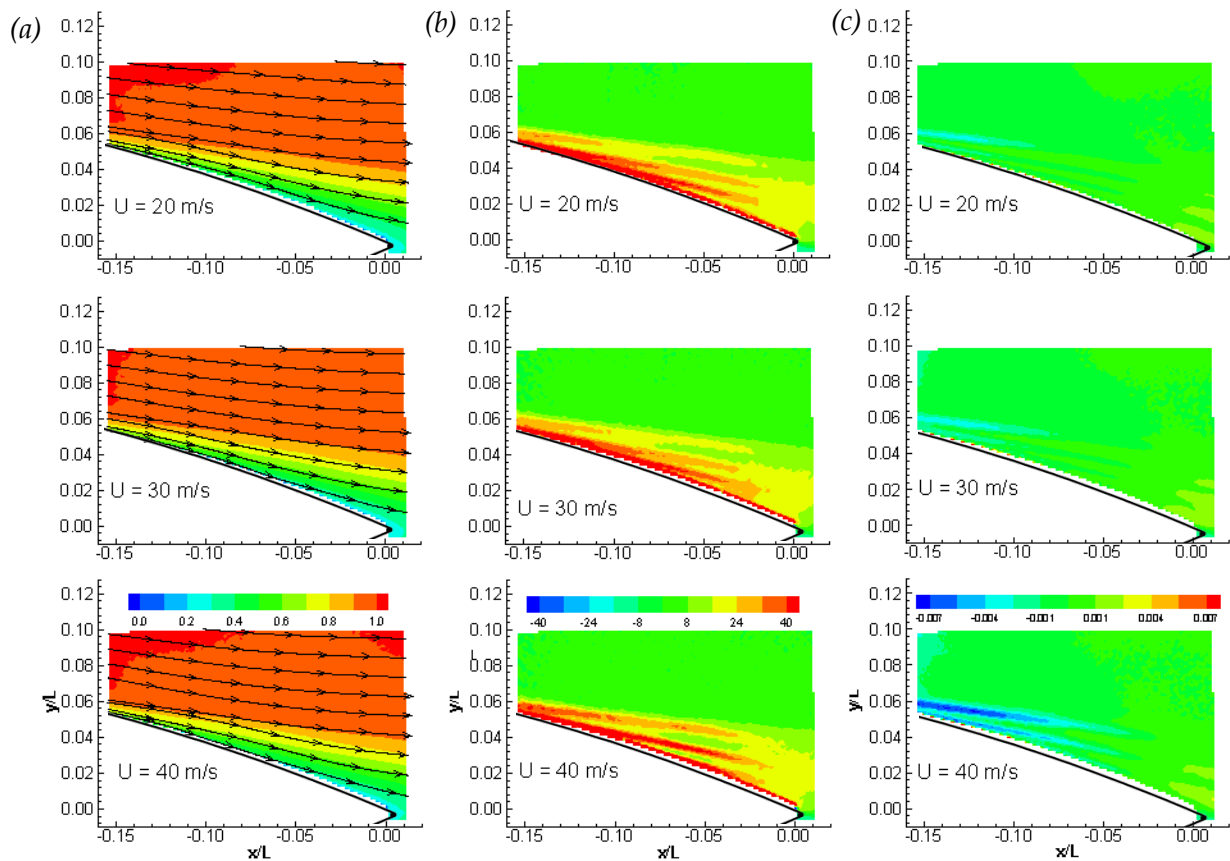


Figure 18 – Ensemble-averaged, (a) non-dimensional streamwise velocity ( $\bar{u}/U_\infty$ ), (b) non-dimensional out-of-plane vorticity ( $\bar{\omega}_z L/U_\infty$ ), (c) Reynolds stress ( $-\overline{u'v'}/U_\infty^2$ ) contours for field-of-view 1,  $\alpha = 0^\circ$  and for freestream velocities of 20, 30 and 40 m/s.

### 4.3 Comparison of Experimental and Computational Results

As part of the verification and validation of the PIV data, the experimental results were compared with available computational fluid dynamics (CFD) results [19]. The CFD model of the generic submarine including the support fairing and pitch actuator arm is shown in Figure 19. To reduce the complexity of the CFD model the wind tunnel test section, the central vertical support pylon connecting the support fairing with the model, and the pitch strut vertical linkage were not modelled. Whilst the CFD simulation is a simplification of the experimental setup, it was shown in Quick *et al.* [1] that the forces predicted correlate well with the experimental results.

In the CFD model an unstructured tetrahedral mesh was used, with the addition of a prism layer near the surface to capture the boundary layer. An initial cell height of 0.001 m coupled with a radial growth rate of 1.15 using 20 prism levels was deemed sufficient to capture the boundary layer development [20]. The average surface cell  $y^+$  value was approximately 80 and the mesh size was approximately  $1 \times 10^6$  cells. A standard k- $\omega$

turbulence model was used with a wall function approach. The computational analysis assumed a fully turbulent boundary layer.

For the model at  $\alpha = 10^\circ$  a comparison between CFD and PIV derived non-dimensional streamwise velocity, vorticity and Reynolds stress are made in Figure 20, Figure 21 and Figure 22, respectively. For the non-dimensional streamwise velocity a good qualitative agreement is evident with both results displaying similar flow features. However, the wake in the PIV plots is broader and extends further downstream. Differences in the vorticity and Reynolds stress are more notable, with the PIV measurements indicating larger concentrated regions and higher turbulence in the wake of the model. Discrepancies may be attributed to inaccuracies and uncertainties in both methods. One notable discrepancy is the central vertical support pylon, which was not modelled in the CFD and may account for some of the differences observed between the two results.

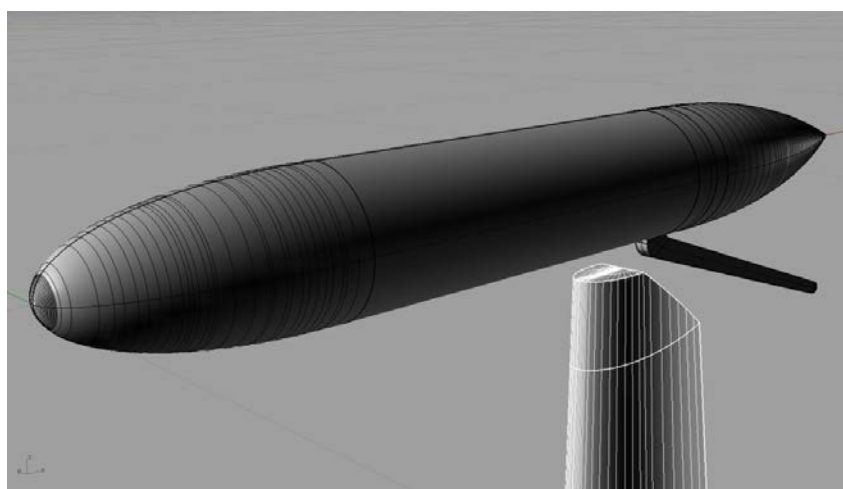


Figure 19 – The CFD surface model of the generic submarine including the support fairing and actuator arm [19]

To provide a quantitative comparison between the PIV and CFD results, profiles were extracted at  $x/L = -0.059, -0.02, 0.011$  and  $0.05$  relative to the tail tip for the model at  $\alpha = 0^\circ$ . Figure 23 presents plots of the mean non-dimensional streamwise velocity at these four locations for the model at  $\alpha = 0^\circ$ . The error bands represent the uncertainty in the mean flow PIV measurements (refer to Appendix C for the uncertainty analysis). Overall the streamwise velocity profiles compare well. The streamwise velocity predicted by CFD is less than that measured using PIV, except for  $x/L = 0.05$  which shows an underestimate of the turbulence quantities in the wake region. For  $x/L = -0.059$  and  $-0.02$  the largest difference is observed near the wall, where the velocity gradients and therefore the PIV bias uncertainties are greatest.

Figure 24 presents the mean non-dimensional out-of-plane vorticity at the same four locations. The oscillatory nature of the PIV profiles is not evident in the CFD results, however the CFD profiles do fall within the experimental error bands of the PIV results. The oscillatory behaviour is likely due to the relatively large uncertainty in the PIV vorticity measurements (see Appendix C). Further investigation is required to ascertain if this behaviour is physical.

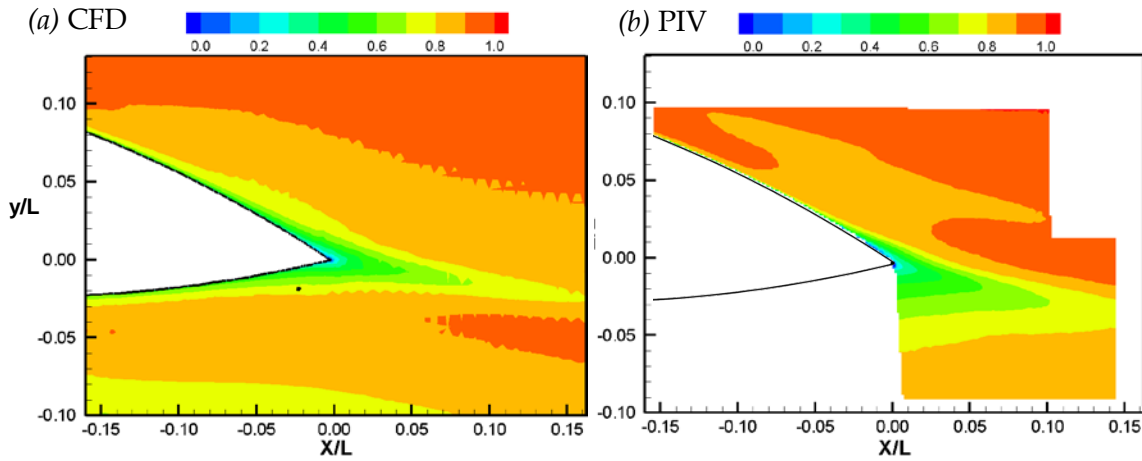


Figure 20 – Comparison between CFD generated non-dimensional streamwise velocity ( $\bar{u}/U_\infty$ ) and PIV results, at  $\alpha = 10^\circ$

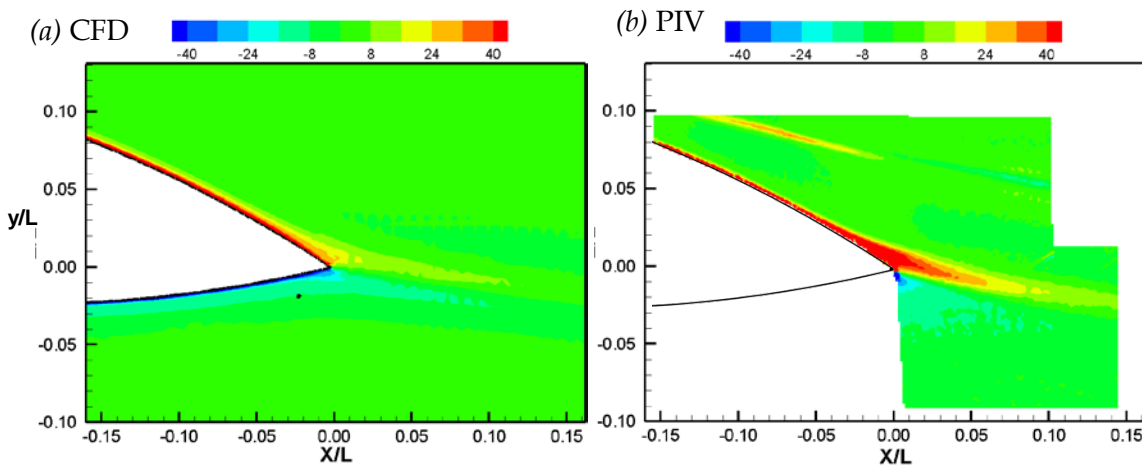


Figure 21 – Comparison between CFD generated non-dimensional out-of-plane vorticity ( $\bar{\omega}_z L/U_\infty$ ) and PIV results, at  $\alpha = 10^\circ$

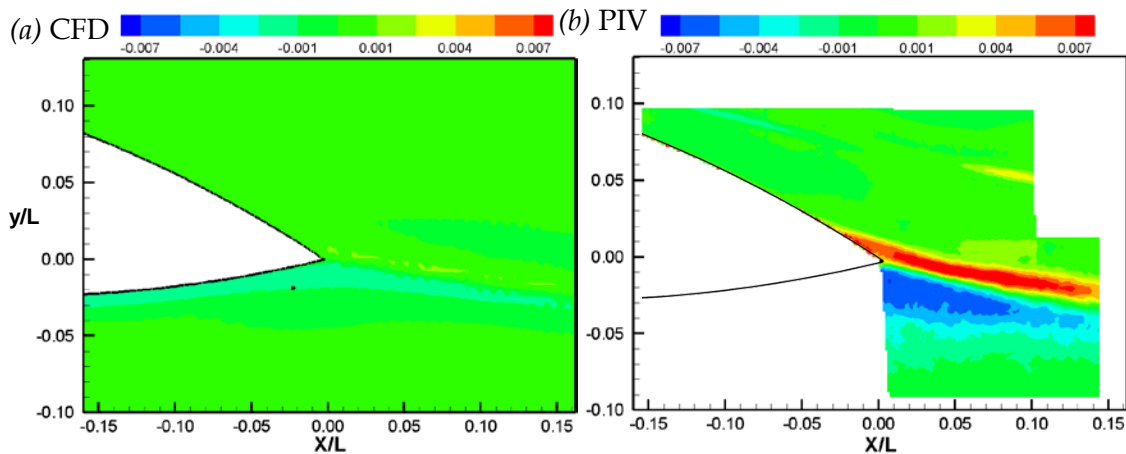


Figure 22 – Comparison between CFD generated Reynolds stress ( $-\overline{u'v'}/U_\infty^2$ ) contours and PIV results, at  $\alpha = 10^\circ$

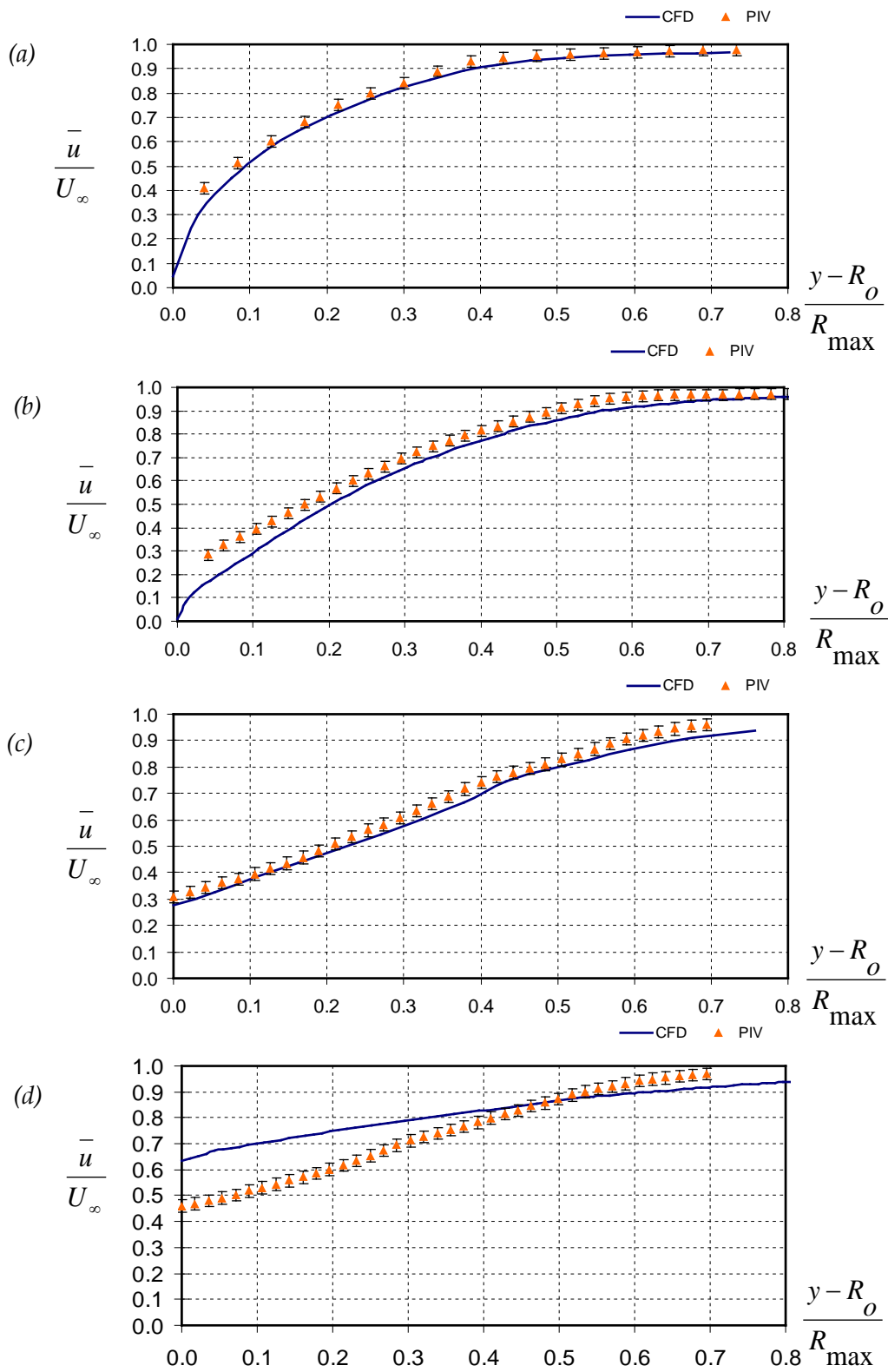


Figure 23 – CFD and PIV non-dimensional streamwise velocity profiles at  $\alpha = 0^\circ$ , at locations, (a)  $x/L = -0.059$ , (b)  $x/L = -0.02$ , (c)  $x/L = 0.011$  and (d)  $x/L = 0.05$

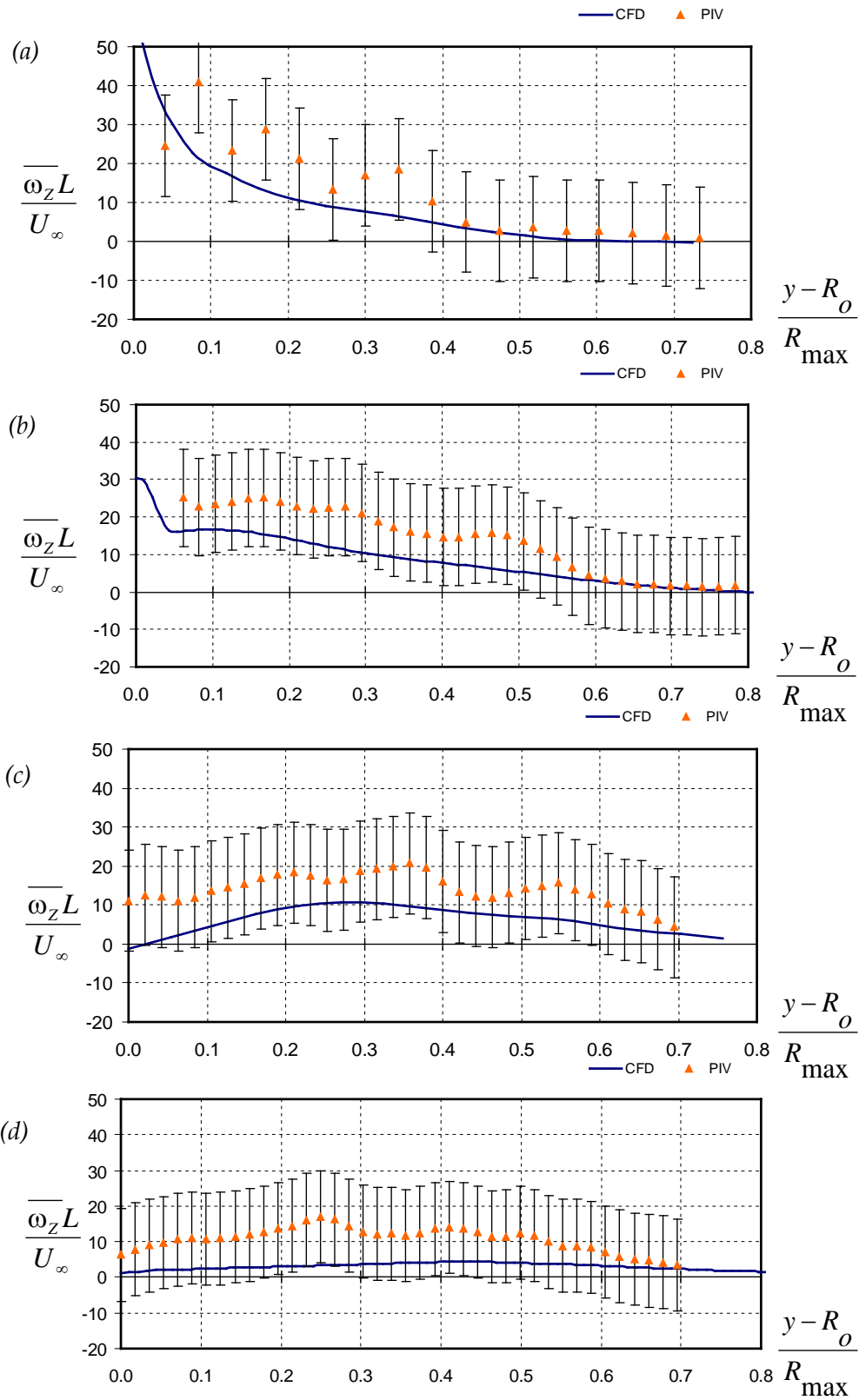


Figure 24 – CFD and PIV non-dimensional out-of-plane vorticity profiles at  $\alpha = 0^\circ$ , at locations (a)  $x/L = -0.059$ , (b)  $x/L = -0.02$ , (c)  $x/L = 0.011$  and (d)  $x/L = 0.05$

## 4.4 Assessment of Data Quality

### 4.4.1 Measurement Uncertainties

The measurement uncertainties in the instantaneous, mean and fluctuating velocity components were calculated using the approach described in [21] and are listed in Table 3. The uncertainties in the mean and fluctuating velocity components are based on random variable analysis for a 95% confidence interval. The vertical velocity component ( $v$ ) is assumed to have identical uncertainty as the streamwise velocity component ( $u$ ). The uncertainties presented are of the same order as those in other published PIV data [22]. A detailed PIV uncertainty analysis is presented in Appendix C.

Table 3 – Uncertainty of the normalised instantaneous and ensemble-averaged velocity, out-of-plane vorticity and Reynolds stress

$U_\infty$ (m/s)	N	Uncertainty			
		$E_{\frac{u}{U_\infty}}$	$E_{\frac{\bar{u}}{U_\infty}}$	$E_{\frac{\omega_z L}{U_\infty}}$	$E_{\frac{\overline{u'v'}}{U_\infty^2}}$
30	1000	$\pm 7.4 \times 10^{-3}$	$\pm 2.4 \times 10^{-2}$	$\pm 1.3 \times 10^1$	$\pm 9.1 \times 10^{-2}$

Increasing the spatial resolution is an effective way to reduce the uncertainty in the PIV measurements. For example improving the spatial resolution by a factor of two (i.e. an image magnification increase of 50%) will decrease the instantaneous axial velocity uncertainty by approximately 40%. A higher spatial resolution can be achieved by mounting the same camera inside the test section of the wind tunnel or by using a lens with a longer focal length. The drawback with either of these approaches would be the reduced field-of-view and therefore in order to achieve the same viewing area more field-of-views would be needed to be blended together.

The uncertainty in the mean parameters can be reduced by taking more samples, N. Assuming the standard deviation in the velocity measurements remains the same, taking 3000 samples instead of 1000 would reduce the uncertainty in the mean velocity, vorticity and Reynolds stress by approximately 40% (refer to Appendix C).

### 4.4.2 Convergence of Mean Flow Parameters

The convergence of the mean flow was assessed qualitatively by plotting a running average for each flow parameter. Plots of the running average of the streamwise velocity,  $u$ , and the vertical velocity,  $v$ , for  $\alpha = 15^\circ$  and field-of-view 3, at a location  $\{x/L, y/L\} = \{-0.0280, 0.0025\}$  relative to the tail tip, are shown in Figure 25. The mean velocities stabilise and approach an approximately constant value after  $\sim 200$  samples. With increasing sample size, the mean velocities remain statistically stationary in time with no accumulative bias uncertainty evident in the mean. The normalised  $u$ -component velocity fluctuation ( $\overline{u'}/U_\infty$ ),  $v$ -component velocity fluctuation ( $\overline{v'}/U_\infty$ ) and Reynolds stress ( $\overline{u'v'}/U_\infty$ ) running averages are also presented in Figure 25, and stabilise after approximately 500 samples.

The convergence of the data at several other locations in the flow was also examined, including, near the surface of the model and in the wake region. Similar behaviours were observed, with convergence of all parameters occurring within approximately 500 samples. These results further validate that the number of image fields taken (approximately 1000) for each test case was adequate in establishing convergence in the statistical parameters.

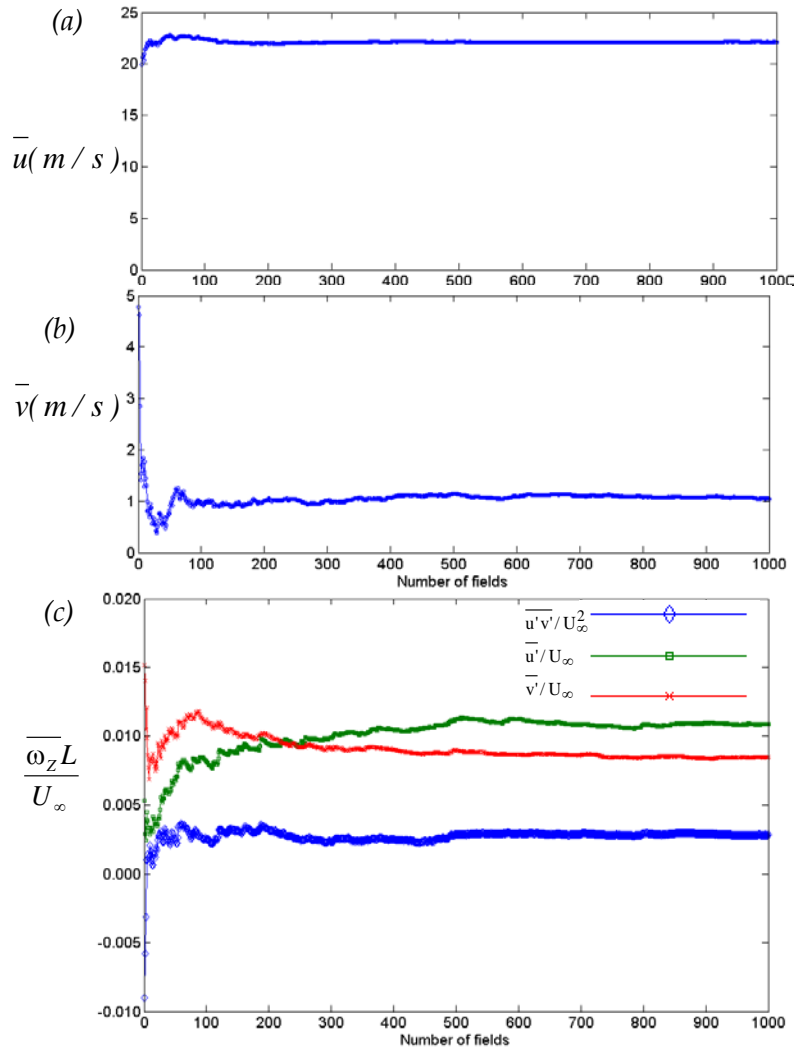


Figure 25 – Running average plots of (a) streamwise velocity ( $\bar{u}$ ), (b) vertical velocity ( $\bar{v}$ ) and (c) normalised u-component velocity fluctuation ( $\bar{u}'/U_\infty$ ), v-component velocity fluctuation ( $\bar{v}'/U_\infty$ ) and Reynolds stress ( $\overline{u'v'}/U_\infty^2$ ) at  $\alpha = 15^\circ$  for field-of-view 3 at  $\{x/L, y/L\} = \{-0.0280, 0.0025\}$ .

#### 4.4.3 Assessment of Peak-Locking

Following the procedure in Raffel *et al.* [4], for the image capture settings used in this study (i.e. lens f-stop of 8 and a reproduction ratio of 6.67), the diffraction limited particle image diameter was estimated to be 1.33 pixels. Peak-locking was assessed by plotting

histograms of particle displacement. Figure 26 is a typical histogram plot showing the particle displacement counts at  $\alpha = -2.5^\circ$ . The displacement counts are not biased towards integer pixel values indicating peak-locking was not present. The histogram plots from the other test cases also showed an acceptable distribution.

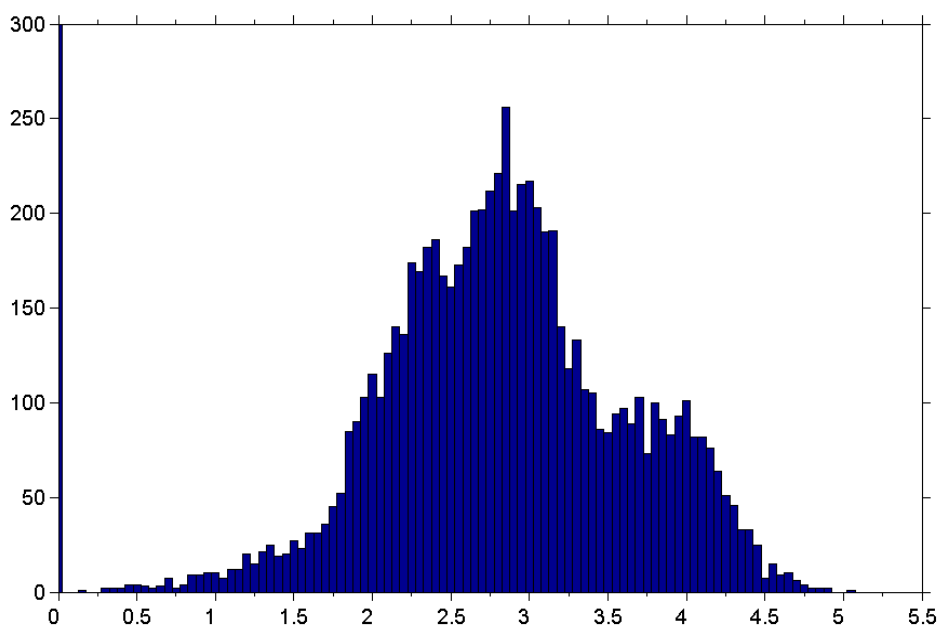


Figure 26 – Histogram of PIV displacement data at  $\alpha = -2.5^\circ$  and field-of-view 3, indicating unbiased pixel displacement. Histogram bin-width = 0.05 pixel.

## 4.5 Lessons Learnt and Key Recommendations

PIV is a new technique being employed in the DSTO experimental facilities, and its implementation in a large-scale facility such as the LSWT presents a number of technical challenges. This section reports the lessons learnt during these tests, with a view towards providing guidance and improvements for future test campaigns.

### 4.5.1 Surface Reflections

The high laser light intensities used in the experiment produce strong reflections which, in some cases, resulted in invalid measurement regions close to the surface of the model. The strong reflections, if directed back towards the lens, also have the potential to destroy the pixel elements in the CCD camera. Furthermore, the reflected light could illuminate particles outside the incident light sheet resulting in spurious measurements.

The submarine model was not specifically designed for PIV. The aluminium surface was polished and then anodised resulting in a highly reflective surface finish. Initial tests at low laser power levels revealed that significant image flaring in regions near the model surface. Furthermore, due to the curvature of the tail, reflections towards the CCD camera were of particular concern. In order to avoid direct reflections back to the camera the laser sheet was shifted in the starboard direction (positive z-direction) away from the centre-line

of the model by approximately 1 mm. This reduced the image flare-up near the surface of the model. For future PIV test campaigns, the model surface should be bead blasted before anodising to ensure a matt finish in order to reduce effects of surface reflections.

#### 4.5.2 Optical Quality of Test Section Window

Initial PIV shakedown tests highlighted the poor optical quality of the LSWT working section window. This proved to be an impediment in obtaining consistent high quality PIV data. The poor optical quality of the window produced optical distortions and are most likely due to an inhomogeneous material, varying thickness of the glass, and surface curvature. The test section window also contained a number of scratches and marks. Taking PIV measurements through these regions of poor optical quality can result in the olive oil seed particles appearing out-of-focus. This reduces the resultant cross-correlation peak-to-noise ratio and produces a high proportion of invalid data in these areas.

Due to the poor optical quality of the LSWT test section window the following procedural changes were adopted:

1. The camera was initially positioned at a desired location such that the field-of-view corresponded to one of the regions of interest depicted in Figure 4.
2. An initial measurement was then taken and the quality of the PIV data was assessed. For the majority of test cases this initial measurement produced unsatisfactory PIV data with large areas of invalid data (e.g. the spurious vector count was greater than 5%).
3. The camera was then translated on the traverse to a new location and the measurements repeated. The camera was moved until the window was of sufficient optical quality to produce good PIV measurements (i.e. the spurious vector count was less than 5%).

For some cases it was not possible to obtain satisfactory PIV measurements over the entire field-of-view. In these cases the regions of the image which consistently produced spurious vectors were masked out.

In future PIV test campaigns the replacement of the test section windows using a material with better optical grade is recommended. Candidate materials include float glass or aircraft grade Plexiglas; the exact specification and quality of such materials and their suitability for the current application is matter for further investigation.

#### 4.5.3 Seeding Losses

The DSTO LSWT is open to atmospheric pressure and therefore seeding losses can occur due to leakage through gaps in the circuit. Losses also occur by oil depositing on exposed surfaces such as the model surface, support structure, tunnel walls, turning vanes, screen and the fan.

Raffel *et al.* [4] showed that the number of particles in each IW must be greater than 8-12 to ensure the valid detection probability exceeds 95% and therefore these losses have the potential to degrade the quality of the PIV data. The operation of the seeding system showed direct correlation with the amount of spurious vectors in the PIV results. Figure 27

shows two plots of the spurious vector count over the number of fields taken at (a)  $\alpha = 0^\circ$  and (b)  $\alpha = 5^\circ$ . At  $\alpha = 0^\circ$ , the seeding system was deliberately toggled ON and OFF and as a consequence the spurious vector count shows distinct peaks and troughs. At  $\alpha = 5^\circ$ , the seeding system remained ON during the entire run and as a consequence the spurious vector count remains low. For the test conditions ( $U_\infty = 30$  m/s) and the seeding system ON during the entire image capture sequence, seeding losses were accounted for and adequate seeding remained inside the tunnel without over saturation. These results show that in order to obtain consistently good quality PIV measurements, for a range of test conditions, it is necessary for the seeding concentration to be monitored such that the minimum acceptable level can be maintained.

After several days of testing the test section walls and the model surface were covered with a film of oil residue. Testing at wind tunnel velocities greater than 30 m/s resulted in increased rate of oil deposition on the tunnel surfaces resulting in significant seeding losses. Seeding improvements may be achieved via local seeding injection or an upstream rake. Both of these methods are intrusive and their effects on the flow-field would need to be assessed. In order to avoid oil build up on exposed surfaces, other seeding alternatives should be investigated. One alternative to olive oil seeding is Di-Ethyl-Hexyl-Sebacate (DEHS) which is a non-soluble liquid suitable for producing aerosols and has been used for PIV seeding in other international large-scale facilities [4] and subject of further investigation.

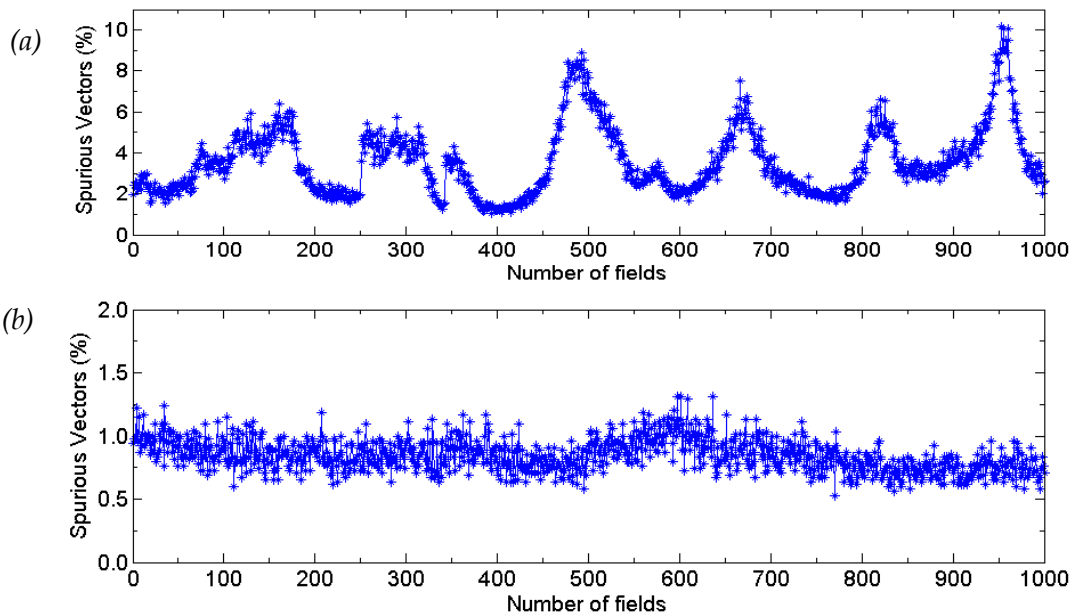


Figure 27 – Plot of spurious vector count over the number of fields taken at (a)  $\alpha = 0^\circ$  and (b)  $\alpha = 5^\circ$ , for field-of-view 1 at a freestream airspeed of 30 m/s.

## 5. Conclusions

DSTO researchers have utilised the complimentary techniques of smoke flow visualisation and PIV to investigate the flow-field over a generic submarine model tested in the LSWT. Smoke flow visualisation revealed the large-scale structure of the flow-field around the model. The flow-field was characterised by cross-flow separation that forms near the tail, and migrated forward with increasing incidence.

The PIV technique provided mean flow-fields, vorticity maps and contour plots of Reynolds stress at targeted areas of interest. With increasing incidence, the streamlines over the upper surface were vectored down along the surface. The PIV results showed flow features consistent with the flow visualisation results. The PIV vorticity contours showed that with increasing incidence, the boundary layer vorticity on the upper surface extended further downstream.

Both the flow visualisation and PIV measurements showed that the model mounting arrangement produced flow disturbance on the underside of the model. Despite this interference the large-scale flow features were consistent with those reported for the flow over a prolate spheroid.

The PIV results were compared with CFD results and a reasonable agreement in the streamwise velocity and vorticity were obtained. Given that both techniques produced similar results, the comparison with CFD was both informative and served to validate the experimental method.

The PIV testing provided insight into the complexities involved in obtaining PIV measurements in a large-scale wind tunnel facility. Practical limitations of the current PIV technique and the facility dictated the test conditions for which good measurements could be acquired. The optical quality of the test section window was highlighted as a deficiency in the experimental setup, as was the importance of consistent seeding, in obtaining high quality PIV results.

A range of improvements have been suggested which are currently being implemented. With these refinements applied to the PIV test technique, researches are confident that an enhanced PIV capability will be provided for future test campaigns.

## 6. Acknowledgements

The authors acknowledge Howard Quick for assistance with the smoke flow visualisation and Andrew Snowden for performing the CFD simulations. Chetan Kumar and Ronny Widjaja for the development of the image stitching software used to blend together the multiple PIV field-of-views. Thank you also to Adam Blandford, Stephen Lam, John Clayton and Jim Nicholls for their contributions.

## 7. References

- [1] Quick, H., Widjaja, R., Anderson, B., Woodyatt, B., Snowden, A. and Lam, S., "Phase I Experimental Testing of a Generic Submarine Model in the DSTO Low Speed Wind Tunnel", Defence Science and Technology Organisation, Client Report, DSTO-TN-1101, 2012.
- [2] Erm L. P., "Calibration of the Flow in the Extended Test Section of the Low-Speed Wind Tunnel at DSTO", Defence Science and Technology Organisation, Technical Report, DSTO-TR-1384, 2003.
- [3] Braslow, A. L. and Knox, E. C., "Simplified Method of Determination of Critical Height of Distributed Roughness Particles for Boundary Layer Transition at Mach Numbers from 0 to 5", NACA TN 4363, 1958.
- [4] Raffel, M., Willert, C. and Kompenhans, J., "Particle Image Velocimetry - A Practical Guide", Springer, New York, 1998.
- [5] Dantec dynamics A/S. Skovlunde, Denmark. Accessed 12 October 2011, <http://www.dantecdynamics.com>
- [6] Adrain, R. J. and Westerweel, J., "Particle Image Velocimetry", Cambridge, New York, 2011.
- [7] Etebari, A. and Vlachos, P. P., "Improvements on the Accuracy of Derivative Estimation from DPIV Velocity Measurements", *Exp. Fluids*, **39**, 2005, pp. 140-1050.
- [8] Liang, D. F., Jiang, C. B. and Li, Y. L., "Cellular Neural Network to Detect Spurious Vectors in PIV Data", *Exp. Fluids*, **34**, 2003, pp. 52-62.
- [9] Christensen, K. T., "The Influence of Peak-Locking Errors on Turbulence Statistics Computed from PIV Ensembles", *Exp. Fluids*, **36**, 2004, pp. 484-497.
- [10] Kumar, C., Widjaja, R., Giacobello, M. and Manovski, P., "PIV Image Blending using MATLAB", DSTO Technical Note, in preparation.
- [11] Felice, D. F. and Pereira, F., "Developments and Applications of PIV in Naval Hydrodynamics", *Particle Image Velocimetry, Topics in Applied Physics*, **112**, 2008, pp. 475-503.
- [12] Han, T. and Patel, V. C., "Flow Separation on a Spheroid at Incidence", *J. Fluid Mech.*, **92**, 1979, pp. 643-657.
- [13] Patel, V. C. and Han, T. "Topology of Laminar Flow on a Spheroid at Incidence", *Comp. Fluids*, **23**, 1994, pp. 939-953.
- [14] Maskell, E. C., "Flow Separation in Three-Dimensions", Royal Aircraft Establishment, RAE Report Aero. 2565, 1955.
- [15] Wang, K. C., "Separation Patterns of Boundary Layer over Inclined Body of Revolution", *AIAA J.*, **10**, 1972, pp. 1044-1050.
- [16] Chesnakas, C. J. and Simpson, R. L., "Detailed Investigation of the Three-Dimensional Separation about a 6:1 Prolate Spheroid", *AIAA Journal*, **35**, 1997, pp. 990-999.

- [17] Ahn, S., "An Experimental Study of Flow Over a 6 to 1 Prolate Spheroid at Incidence", Ph.D. Thesis, Virginia Polytechnic Institute and State University, 1992.
- [18] Wetzel, T. G., Simpson, R.L. and Chesnakas, C.J., "Measurement of Three-Dimensional Crossflow Separation", *AIAA J.*, **36**, 1998, pp. 557-564.
- [19] Snowden, A. D., Private communication, 21 June 2011.
- [20] Snowden, A. D. and Widjaja, R., "Computational Fluid Dynamics Modelling of the Defense Advanced Research Projects Agency SUBOFF Submarine Model in Bare Hull Configuration", Defence Science and Technology Organisation, Technical Report, DSTO-TR-2551, 2011.
- [21] Kostas, J., "An experimental Investigation of the Structure of a Turbulent Backward Facing Step Flow", PhD thesis, Monash University, Melbourne, Australia, 2002.
- [22] Murray, N. E. and Ukeiley, L. S., "An Application of Gappy POD for Subsonic Cavity Flow PIV Data", *Exp. Fluids*, **42**, 2007, pp. 79-91.
- [23] Edwards C.D., "Calibration of the Reference Velocity in the Test Section of the Low Speed Wind Tunnel at the Aeronautical and Maritime Research Laboratory" Defence Science and Technology Organisation, Technical Note, DSTO-TN-0248, 2000.
- [24] Lam, S. S. "Calibration Report - Low Speed Wind Tunnel Static Pressure Transducer". DSTO Low Speed Wind Tunnel Calibration Report, AVD-LSWT-CAL1202, Jan 2012.
- [25] Lam, S. S. "Calibration Report - Low Speed Wind Tunnel Flow Reference Differential Pressure Transducer". DSTO Low Speed Wind Tunnel Calibration Report, AVD-LSWT-CAL1201, Jan 2012.
- [26] Bruun, H. H., *Hot-wire anemometry Principles and Signal Analysis*, Oxford Science Publications, 1995.
- [27] Taylor, J. R., *An introduction to Error Analysis - the study of uncertainties in physical measurements*, 2nd Edition, Universal Science Books, 1982.

## Appendix A: Wind Speed Measurement

The DSTO LSWT flow reference instrumentation was used for measurement of the tunnel static, the differential pressure across the contraction and the tunnel temperature. These measurements are used to calculate the test section wind speed and Reynolds number.

The differential pressure is obtained by measurement of the pressure between two piezometer rings located at the entrance and exit of the tunnel contraction. The pressure is sampled by a 3 PSID range Digiquartz differential pressure transducer. A calibration factor (1.079) is applied as a correction to the pressure measurement obtained from the two piezometer rings to represent accurately the correct dynamic pressure and consequently, velocity, at the centre of the test section midway between the centres of the turntables in the floor and ceiling [23]. The static pressure in the test section is measured by an absolute 23 PSIA Digiquartz pressure transducer. The tunnel temperature is measured by an Intech LPN-R RTD temperature transmitter in combination with a 3 wire Platinum Pt100 RTD temperature transducer.

### A.1. Wind Speed Measurement Uncertainty

The measured parameters required to estimate the wind speed in the test section of the LSWT are

- $p_d$  = Differential pressure across the piezoelectric rings (Pa),
- $P_s$  = Static pressure of the test section (Pa),
- $T$  = Test section temperature (K).

Other parameters required in the calculation of the wind speed are

- $\rho$  = Density of air in the test section ( $\text{kg}\cdot\text{m}^{-3}$ ),
- $k$  = Wind speed calibration factor of the tunnel = 1.079 [23],
- $R$  = Ideal gas constant for air =  $287 \text{ (J}\cdot\text{kg}^{-1}\text{K}^{-1})$ .

The wind speed or freestream airspeed,  $U_\infty$  is calculated according to the equation,

$$U_\infty = \sqrt{\frac{2kP_d}{\rho}}. \quad (\text{A.1})$$

Where the air density,  $\rho$ , is evaluated according to the ideal gas equation,

$$\rho = \frac{P_s}{RT}. \quad (\text{A.2})$$

The uncertainty in  $U_\infty$  is then estimated by combining the differential pressure uncertainty,  $E_{Pd}$ , the wind speed calibration factor uncertainty,  $E_k$ , and the uncertainty in the density,  $E_\rho$ ,

$$E_{U_\infty} = \sqrt{\left(\frac{\partial U_\infty}{\partial P_d} E_{Pd}\right)^2 + \left(\frac{\partial U_\infty}{\partial k} E_k\right)^2 + \left(\frac{\partial U_\infty}{\partial \rho} E_\rho\right)^2}, \quad (\text{A.3})$$

or, when simplified,

$$E_{U_\infty} = \sqrt{\left(\frac{kE_{Pd}^2}{2\rho P_d}\right) + \left(\frac{P_d E_k^2}{2\rho k}\right) + \left(\frac{kP_d E_\rho^2}{2\rho^3}\right)}, \quad (\text{A.4})$$

where the uncertainty in the density is estimated by combining the statics pressure uncertainty,  $E_{Ps}$  and the tunnel temperature uncertainty,  $E_T$ ,

$$E_\rho = \sqrt{\left(\frac{\partial \rho}{\partial P_s} E_{Ps}\right)^2 + \left(\frac{\partial \rho}{\partial T} E_T\right)^2} = \sqrt{\left(\frac{E_{Ps}}{RT}\right)^2 + \left(-\frac{P_s}{RT^2} E_T\right)^2}. \quad (\text{A.5})$$

For typical tunnel conditions, the uncertainties based on random variable analysis for a 95% confidence interval, that is a uncertainty coverage factor of 2, are as follows,

$$\begin{aligned} P_s &= 101325 \text{ Pa}, & E_{Ps} &= \pm 6.10 \text{ Pa [24]}, \\ T &= 300 \text{ K}, & E_T &= \pm 0.5 \text{ K (based on a conservative accuracy estimate for a resistance temperature detector),} \\ k &= 1.079, & E_k &= \begin{aligned} &\pm 0.017, \quad U_\infty \leq 20 \text{ m/s,} \\ &\pm 0.003, \quad U_\infty \geq 40 \text{ m/s,} \end{aligned} \quad [23] \\ & & & \text{For 30 m/s, an average of } E_k = \pm 0.01 \text{ is assumed.} \\ E_{Pd} &= 2.18 \text{ Pa [25].} \end{aligned}$$

For the typical tunnel conditions, the wind speed uncertainties for a range of tunnel velocities are shown in Table A1.

Table A1 – LSWT wind speed uncertainties

Wind Speed $U_\infty$ (m/s)	Differential Pressure $P_d$ (Pa)	Uncertainty $E_{U_\infty}$ (m/s)
5.0	13.6	$\pm 0.40$
20.0	218.1	$\pm 0.19$
30.0	490.8	$\pm 0.16$
40.0	872.5	$\pm 0.08$

## Appendix B: PIV Measurement Settings

Table B1 – Summary of PIV measurement settings

Laser Maximum Pulse Energy	200 mJ
Laser Wavelength	532 nm
Laser Sheet Thickness (at the model surface)	1.5 mm
Camera Resolution	4008 × 2672 pixels
Camera Pixel Size	9 μm × 9 μm
Camera Frame Rate	2.07 Hz
Time Delay ( $\Delta t$ )	6 – 15 μs
Lens Focal Length	200 mm
Spatial Resolution	60.03 μm/pixel
First Interrogation Window Size	64 × 64 pixels
Second Interrogation Window Size	64 × 64 pixels
Overlap between Interrogation Windows	50%
Vector Spatial Resolution	1.92 mm
Seed Particles	Olive Oil
Nominal Particle Size	1 μm
Number of Fields (N)	~1000

*This page is intentionally blank*

## Appendix C: PIV Uncertainty Analysis

### C.1. PIV Measurement Uncertainty

The PIV measurement uncertainties in the instantaneous, mean and fluctuating velocity components were calculated using the approach described in [21]. The total PIV velocity measurement uncertainty,  $E_u$ , is obtained by combining the PIV particle displacement uncertainty ( $E_{disp}$ ), scaling uncertainty ( $E_{scale}$ ) and timing uncertainty ( $E_{time}$ ),

$$E_u^2 = \left( \frac{\delta_u}{u} \right)^2 = E_{disp}^2 + E_{scale}^2 + E_{time}^2 = \left( \frac{\delta_{\Delta X}}{\Delta X} \right)^2 + \left( \frac{\delta_{scale}}{L_{scale}} \right)^2 + \left( \frac{\delta_{\Delta t}}{\Delta t} \right)^2. \quad (C.1)$$

The theoretical minimum resolvable pixel displacement,  $\delta_{\Delta x}$ , for the PIV algorithm was determined to be 0.05 pixel for the recursive algorithm. This was obtained by processing digitally simulated images with known particle displacement. The values quoted in the literature are of the same order, for example, a minimum resolvable displacement of 0.05 pixel was also attained in [22]. For the image capture settings used in this study, a freestream velocity of 30 m/s and a time delay,  $\Delta t = 10 \mu s$  corresponds to a displacement of 5 pixels ( $\Delta X$ ), and therefore the PIV displacement uncertainty expressed as a percentage of the freestream velocity is  $\pm 0.5\%$  (1.0%).

The PIV camera images are calibrated by inserting a ruler in-line with the laser sheet and measuring the number of pixels over a calibration length. For the image calibration, the in-plane scaling uncertainty was estimated to be 2 pixels based on the ability to estimate the centre of the reference graduations on a ruler from an image acquired using the PIV camera. Two graduations need to be chosen over a calibration length thus for each graduations there is 2 pixel uncertainty in both the horizontal and vertical directions. Therefore the combined total in-plane scaling uncertainty is

$$\delta_{scale} = \sqrt{(2^2 + 2^2) + (2^2 + 2^2)} = 4 \text{ pixels.}$$

For the out-of-plane scaling uncertainty an Empire<sup>TM</sup> spirit level was used to align the calibration ruler in both pitch and roll. The accuracy of the spirit level is quoted as 0.5 mm/m thus for the 6" (152.4 mm) spirit level this corresponds to 0.0762 mm (or 0.029°). The projected out-of-plane uncertainty is then equal to

$$152.4 - 152.4 \cos(0.029^\circ) = 1.92 \times 10^{-5} \text{ mm,}$$

and given the magnitude of this uncertainty it was deemed insignificant and was ignored.

The calibration length used was 120 mm. For an image spatial resolution of 60.0  $\mu m$ /pixel this corresponds to 2000 pixels ( $L_{scale}$ ). Thus the total scaling uncertainty is,

$$E_{scale} = \delta_{scale} / L_{scale} = 4 / 2000 = 0.002 = \pm 0.1\% \text{ (total uncertainty} = 0.2\%).$$

This analysis assumes the ruler is calibrated and does not take into account the error of the actual ruler measurement length.

The timing uncertainty is a combination of the minimum clock time of the synchroniser (1 ns) and the laser jitter (1 ns). The combined timing uncertainty for two laser pulses can be calculated,

$$\delta_{time} = \sqrt{(1^2 + 1^2) + (1^2 + 1^2)} = 2 \text{ ns.}$$

For a time delay,  $\Delta t = 10 \mu\text{s} = 10000 \text{ ns}$ , the corresponding timing uncertainty,

$$E_{time} = \delta_{\Delta t} / \Delta t = 2/10000 = \pm 0.0002 = \pm 0.02\% \text{ (total uncertainty} = 0.04\%).$$

The total PIV velocity uncertainty for the  $u$  velocity component is then given by the root-sum-square of each the uncertainties,

$$E_u = \sqrt{E_{disp}^2 + E_{scale}^2 + E_{time}^2} = \sqrt{0.5^2 + 0.10^2 + 0.02^2} \approx \pm 0.51\% (1.02\%).$$

Therefore the normalised instantaneous PIV streamwise velocity ( $u/U_\infty$ ) the corresponding uncertainty is  $\pm 0.0051$ .

The combined PIV streamwise velocity and LSWT freestream airspeed uncertainty is found by a summation in quadrature of the corresponding uncertainties,

$$\begin{aligned} E_{\frac{u}{U_\infty}} &= \sqrt{E_u^2 + \left(\frac{E_{U_\infty}}{U_\infty}\right)^2} = \sqrt{0.0051^2 + \left(\frac{0.16}{30}\right)^2} \\ &= \pm 0.74\% (1.48\%). \end{aligned}$$

Therefore for the normalised instantaneous PIV streamwise velocity ( $u/U_\infty$ ) the combined uncertainty is  $\pm 0.0074$ .

The  $v$  velocity component is assumed to have identical uncertainty as the  $u$  velocity component, i.e.  $E_v = \pm 0.0051$  (0.0102) and  $E_{\frac{v}{U_\infty}} = \pm 0.0074$  (0.0148).

## C.2. Mean Velocity Uncertainty

Velocity measurements obtained from PIV are considered to be statistically independent and conform to a normal distribution [22]. From the theory of random variable analysis, for a 95% confidence interval, the fractional uncertainty in the streamwise ( $u$ ) mean velocity (or the statistical uncertainty) is given by,

$$E_u = \frac{2 \langle \sigma_u \rangle}{U_\infty \sqrt{N}} = \frac{2u_{RMS}}{U_\infty \sqrt{N}}, \quad (\text{C.2})$$

where  $\sigma_u$  is the standard deviation,  $u_{\text{RMS}}/U_\infty$  is the turbulence intensity and  $N$  is the number of samples. The existence of a PIV velocity uncertainty,  $E_{u_r}$ , in each individual measurement is added to the statistical uncertainty,  $E_{\bar{u}}$ , to get the total uncertainty in the mean velocity. The maximum turbulence intensity  $(u_{\text{RMS}}/U_\infty)_{\text{max}}$  was determined from the mean flow-fields and was found to be 0.34, therefore

$$\begin{aligned} E_{\bar{u}} &= \frac{2 \times 0.34}{\sqrt{1000}} \\ &= \pm 2.2\% \text{ (4.4\%)} \end{aligned}$$

The total uncertainty in the streamwise ( $u$ ) mean velocity is then given by the root-sum-square,

$$\begin{aligned} E_{\text{Total } \bar{u}} &= \sqrt{(E_{\bar{u}})^2 + E_{u_r}^2} = \sqrt{(2.2)^2 + 0.51^2} \\ &= \pm 2.3\% \text{ (4.5\%)}. \end{aligned}$$

Therefore for the normalised mean PIV derived velocity  $(\bar{u}/U_\infty)$  the corresponding uncertainty is  $\pm 0.023$ .

The combined normalised mean PIV velocity and freestream airspeed uncertainty is found by a summation in quadrature of the corresponding uncertainties,

$$\begin{aligned} E \frac{\bar{u}}{U_\infty} &= \sqrt{E_{\text{Total } \bar{u}}^2 + \left(\frac{E_{U_\infty}}{U_\infty}\right)^2} = \sqrt{0.023^2 + \left(\frac{0.16}{30}\right)^2} \\ &= \pm 2.4\% \text{ (4.8\%)} \end{aligned}$$

Thus for the normalised mean PIV velocity  $(\bar{u}/U_\infty)$  the corresponding combined fractional uncertainty is  $\pm 0.024$ .

The mean  $v$  velocity component is assumed to have identical uncertainty as the  $u$  mean velocity component.

### C.3. Vorticity Uncertainty

Two uncertainties make up the out-of-plane vorticity uncertainty, the precision (or random) uncertainty and the bias uncertainty [7]. The precision uncertainty represents the uncertainty due to velocity field calculation (i.e. the PIV uncertainty) and the bias uncertainty represents the consistent under-estimation or over-estimation of the vorticity estimation scheme. Both depend on the spatial separation of the data,  $\Delta$ , and on the size of a relevant length scale to be resolved,  $L_c$ , although in an opposing fashion.

The normalised precision uncertainty for the second order finite difference vorticity calculation scheme used in this study may be calculated from [7] as,

$$E_{\omega_{\text{pres}}} = \lambda E_{u_r}, \quad (\text{C.3})$$

where  $E_u$  is the total PIV velocity uncertainty in the streamwise velocity and  $\lambda$  is a non-dimensional precision uncertainty transmission ratio and is given as

$$\lambda = k \frac{L_c}{\Delta}, \quad (\text{C.4})$$

where  $k = 1$  for the second order finite difference scheme. In this analysis it is assumed that the  $v$  velocity component uncertainty is the same as the  $u$  velocity uncertainty.

The normalised peak vorticity bias uncertainty for the second order finite difference scheme can be calculated using [7],

$$E_{\omega_{bias}} = \frac{\omega_{bias}}{\omega_{max}} = \gamma \left( \frac{\Delta}{L_c} \right)^\phi, \quad (\text{C.5})$$

where  $\omega_{max}$  is the peak out-of-plane vorticity calculated from the PIV velocity measurements and  $\omega_{bias}$  is the actual peak out-of-plane vorticity value,  $\gamma = 0.2416$  and  $\phi = 2$  for the second order finite difference scheme.

Thus the total uncertainty in the vorticity is calculated by,

$$E_\omega = \sqrt{E_{\omega_{pres}}^2 + E_{\omega_{bias}}^2}. \quad (\text{C.6})$$

Where the total uncertainty in the vorticity is expressed as fractional uncertainty of the actual out-of-plane vorticity and the peak out-of-plane vorticity calculated from the PIV velocity measurement, i.e.,

$$E_\omega = \left( \frac{\omega_{actual}}{\omega_{max}} \right).$$

Substituting Eq. (C.3) and Eq. (C.5) gives,

$$E_\omega = \sqrt{\left( \frac{L_c}{\Delta} E_u \right)^2 + \left( 0.2416 \left( \frac{\Delta}{L_c} \right)^2 \right)^2}. \quad (\text{C.7})$$

For a  $64 \times 64$  IW size, 50% overlap factor and an image spatial resolution of  $60.03 \mu\text{m}$ , the spatial separation of the data is  $\Delta = 32 \times 0.06003 = 1.92 \text{ mm}$ . The total PIV uncertainty in the streamwise velocity was calculated previously,  $E_u \approx \pm 0.51\%$ .

As a representative case to explore the effect of spatial resolution and the vorticity estimate scheme on the bias and random error, Etabari and Vlachos [7] use an Oseen vortex and defined  $L_c$  as the as length scale of the vortex core. The flow around submarine can be considered a complex flow field with a range of length scales present in the flow, thus a characteristics length scale is difficult to define. A conservative assumption was made and

the characteristic length scale was based on the vorticity thickness at the tail of the model, which is defined as

$$\delta_{\omega_z} = \frac{U_{MAX} - U_{MIN}}{\left(\frac{du}{dy}\right)_{MAX}} = \frac{U_{\infty}}{\left(\frac{du}{dy}\right)_{MAX}}, \quad (C.8)$$

where  $U_{MIN} = 0$  at the surface of the model. The vorticity thickness at the tail of the model was determined to be approximately 21 mm.

Thus the uncertainty in the instantaneous vorticity is

$$\begin{aligned} E_{\omega} &= \sqrt{\left(\frac{21}{1.92} \cdot 0.0051\right)^2 + \left(0.2416 \left(\frac{1.92}{21}\right)^2\right)^2} \\ &= \pm 0.056 \\ &= \pm 5.6\% (11\%) \end{aligned}$$

The fractional uncertainty in the instantaneous vorticity is therefore  $\pm 0.056$  of the maximum PIV measured instantaneous vorticity.

The mean vorticity components were extracted from the mean velocity field and the uncertainty calculation method is thus identical to that explained above. The bias uncertainty remains the same while the precision uncertainty increases in accordance with the greater uncertainty associated with the mean velocity field, i.e.

$$E_{\omega_{\text{corpres}}} = \lambda \left( \sqrt{E_u^2 + E_v^2} \right) \quad (C.9)$$

The value  $\lambda$  is the same as (C.4) and the mean velocity uncertainty in the streamwise velocity was previously calculated,  $E_u = \pm 2.3\%$ , thus the total uncertainty in the mean out-of-plane vorticity is calculated using,

$$E_{\omega} = \sqrt{\left(\frac{L_c}{\Delta} \left(\sqrt{E_u^2 + E_v^2}\right)\right)^2 + \left(0.2416 \left(\frac{\Delta}{L_c}\right)^2\right)^2}. \quad (C.10)$$

Substituting the values,

$$\begin{aligned} E_{\omega} &= \sqrt{\left(\frac{21}{1.92} \times \sqrt{0.0051^2 + 0.023^2}\right)^2 + \left(0.2416 \left(\frac{1.92}{21}\right)^2\right)^2} \\ &= \pm 0.25 \\ &= \pm 25\% (50\%). \end{aligned}$$

The fractional uncertainty in the mean out-of-plane vorticity is calculated to be  $\pm 0.25$  of the maximum measured PIV vorticity.

The combined normalised mean PIV vorticity, model length and freestream airspeed uncertainty is found by a summation in quadrature of the corresponding uncertainties,

$$\begin{aligned} E_{\frac{\omega L}{U_\infty}} &= \sqrt{E_\omega^2 + \left(\frac{E_L}{L}\right)^2 + \left(\frac{E_{U_\infty}}{U_\infty}\right)^2} \\ &= \sqrt{0.25^2 + \left(\frac{0.5}{1350}\right)^2 + \left(\frac{0.16}{30}\right)^2} \\ &= \pm 0.25 \\ &= \pm 25\% (50\%). \end{aligned}$$

where the uncertainty in the model length,  $E_L = \pm 0.5$  mm.

The maximum normalised mean PIV vorticity,  $(\overline{\omega_z}_{MAX} L / U_\infty) \approx 53$  and thus the corresponding mean out-of-plane vorticity uncertainty is  $E_{\frac{\omega L}{U_\infty}} \approx (0.25 \times 53) \approx \pm 13$ .

#### C.4. Reynolds Stress Uncertainty

The normal stresses,  $\overline{u'^2}$  and  $\overline{v'^2}$  are related to the standard deviation of each velocity components as follows,

$$\overline{u'^2} = \sigma_u^2, \quad (C.11)$$

$$\overline{v'^2} = \sigma_v^2, \quad (C.12)$$

and from the theory of propagation of uncertainties [26], their associated fractional uncertainties are

$$E_{\overline{u'^2}} = 2E_{\sigma_u}, \quad (C.13)$$

$$E_{\overline{v'^2}} = 2E_{\sigma_v}. \quad (C.14)$$

For a 95% confidence interval the corresponding fractional uncertainty in the standard deviation of the velocity may be written [27],

$$E_{\sigma_u} = \frac{2}{\sqrt{2(N-1)}}, \quad (C.15)$$

$$E_{\sigma_v} = \frac{2}{\sqrt{2(N-1)}}. \quad (C.16)$$

The values of  $E\sigma_u$  and  $E\sigma_v$  are thus independent of the sample's standard deviation and merely a function of sample size [27]. The Reynolds shear stress is considered to have similar uncertainties associated with them and the uncertainties associated with the velocity components can be considered equal, i.e.  $E_{\bar{u}^2} = E_{\bar{v}^2} = E_{\overline{u'v'}}$ , therefore,

$$E_{\overline{u'v'}} = \frac{4}{\sqrt{2(N-1)}}. \quad (\text{C.16})$$

Thus for a sample size of  $N = 1000$ , the uncertainty in the ensemble-averaged Reynolds stress (and normal stresses) is  $\pm 9\%$  (total uncertainty = 18%) as a percentage of the measured value. Thus for the fractional uncertainty of the PIV derived normalised Reynolds stress,  $\left(\frac{\overline{u'v'}}{U_\infty^2}\right)$ , the corresponding uncertainty is  $\pm 0.09$ .

The combined normalised PIV Reynolds Stress and freestream airspeed uncertainty is found by,

$$\begin{aligned} E \frac{\overline{u'v'}}{U_\infty^2} &= \sqrt{\left(E_{\overline{u'v'}}\right)^2 + \left(\frac{2E_{U_\infty}}{U_\infty}\right)^2} \\ &= \sqrt{0.09^2 + \left(\frac{2 \times 0.16}{30}\right)^2} \\ &= \pm 0.091 \\ &= \pm 9.1\% (18.2\%). \end{aligned}$$

Thus for the normalised Reynolds stress,  $\left(\frac{\overline{u'v'}}{U_\infty^2}\right)$ , the corresponding combined fractional uncertainty is  $\pm 0.091$ .

